Segment Reconstruction in Drift Tube Chambers with the Legendre Transform

A dissertation presented

by

Michail S. Bachtis

to

The Department of Physics

in partial fulfillment of the requirements

for the degree of

Master of Science

in the subject of

Physics

National Technical University

Athens, Greece

July 2007

Thesis advisor
Theo Alexopoulos

Author
Michail S. Bachtis

Abstract

Track reconstruction is a common research subfield in experimental High Energy Physics as well as in other research areas. High energy physics experiments consist of several types of sub-detectors which need to be combined to provide an efficient measurement. Moreover, because of the nature of the investigated interactions, the tracking parameters must be specified with very high accuracy. For these reasons, high performance algorithms are being used to provide high reconstruction efficiency, low number of fake-reconstructed tracks and high resolution. In this thesis, a new reconstruction method was developed for track reconstruction in Drift tube chambers. Drift tube chambers dominate in muon detection during the last 30 years. During the last decade there have been numerous attempts to replace them with newer technologies (Silicon Drift Detectors, MicroMegas, etc). The arsenal of track reconstruction techniques is very large. Hough transforms, Combinatorics, Projecting techniques, Elastic tracking, Kalman filters and many other algorithms have been studied and applied. This study describes the application of a novel method based on the Legendre transform. The Legendre transform is very commonly used in theoretical physics (for example in Thermodynamics and Analytical Mechanics). In this application its geometrical properties are utilized. Drift tube chambers provide a set of drift circles as signal and the particle tracks are found by finding the common tangent lines to these circles. The Legendre transform of a convex or concave function provides all the tangent lines to the function. According this principle, for each drift circle a new space (the space of tangents) is created. The common points on this new space represent the tangent lines. The method was tested in standalone controlled Monte carlo environment for a study of its full properties. Furthermore, the algorithm was applied to the new and under commissioning Monitored Drift Tube (MDT) chambers of the ATLAS experiment.

Contents

Title Page i
Abstract iii
Table of Contents iv
List of Figures vi
List of Tables viii
Acknowledgments ix
Dedication x

1 The ATLAS Detector **1**
1.1 The Atlas Coordinate System 2
1.2 Inner Detector 2
1.3 Calorimetry 3
1.4 Muon Spectrometer 4
1.4.1 Muon subdetectors 4
1.4.2 Muon Reconstruction 5
1.4.3 Performance of Muon Spectrometer 6

2 MDT Chamber Physics and Technology **11**
2.1 Physics of drift tube chambers 13
2.1.1 MDT Operation in ATLAS 18
2.2 Construction imperfections and ageing 19
2.2.1 Displacement of the wire 19
2.2.2 Ageing Processes 20

3 The Legendre Transform **23**
3.1 Definition 23
3.2 Examples 25
3.3 The Circle 26
3.4 Properties 28
3.5 Legendre Transform in higher dimensions 29
3.6 Legendre transform of order k 31
3.6.1 Thermodynamic Potentials 32
3.6.2 Lagrange and Hamilton equations 34

4 Pattern Recognition in Drift Tube Chambers **38**
4.1 The MDT chamber reconstruction problem 38
4.2 The Legendre transform approach 39
4.2.1 The Histogram method 39
4.2.2 Selecting the bin size 40
4.2.3 Clustering in the Legendre space 40
4.2.4 Drift circle association and least square fit 42
4.3 Object Oriented implementation 42
4.3.1 Core classes 43
4.3.2 Secondary classes 43
4.4 Performance study 44
4.4.1 Resolution 45
4.4.2 Reconstruction Efficiency and Fake Rate 45
4.4.3 Computing performance 46
4.5 Summary 47

5 A Legendre Segment finder for the ATLAS MDT System **58**
5.1 Description of the Algorithm 58
5.2 Reconstruction performance in the ATLAS simulation framework . . 60
5.2.1 Performance on a $p_t = 20$GeV sample 61
5.2.2 Eliminating cavern background 65
5.2.3 Overall performance 65
5.2.4 Computing performance 66
5.3 Summary 67

A The Radon/Hough transform **68**

Bibliography **70**

List of Figures

1.1 The ATLAS experiment 1
1.2 The ATLAS coordinate system 7
1.3 ATLAS Toroid magnets. (a) Bending power in the barrel, end-cap and transition region (b) Magnetic field map lines in the transverse plane (transition region) (c) Atlas Barrel end end-cap toroid instrumentation 8
1.4 Muon instrumentation of the ATLAS experiment 9
1.5 Muon Reconstruction efficiency for combined and standalone reconstruction. (a) Efficiency vs p_t. (b) p_t resolution. (c) Efficiency vs η. (d) η resolution. (e) Efficiency vs ϕ. (f) ϕ esolution. 10

2.1 A Monitored Drift Tube chamber 11
2.2 Monitored Drift tube and endplug 13
2.3 Drift tube operation in a magnetic field with curved drift path. 18
2.4 Shape of the electric field with and without displaced wire. 20
2.5 Picture taken with an electron microscope of a wire of a tube. The thickness of the layer is about 2μ m 21
2.6 Wire partly reanimated using sputtering in pure argon. Some parts are still covered with a layer of carbon and oxygen, some parts show the gold layer of the wire. The average pulse charge of the wire at this state was about 75% compared to a new one. 22

3.1 The Legendre transform, (a) for a convex and (b) for a concave function. 24
3.2 Some simple functions and their tangential representation that is derived by the Legendre transform 35
3.3 (a) Representation of the circle by a convex and a concave function, (b) Tangent Lines in the canonical form equation, (c) Representation of the circle in Legendre transformation space. The circle corresponds to two sinograms in the Legendre transformation space. 36
3.4 Legendre Transform in two dimensions 37

4.1 Drift circles produced by track and Legendre transform reconstruction principle 48

4.2 (a). θ step while resolving the line (b). Drift error of the MDT Chamber 49
4.3 (a). Example event (Drift circles on track). (b). Legendre space (c). Legendre space (zoom in maximum) (d). Legendre space (polar coordinates) 50
4.4 (a). Legendre space after thresholding. (b). Lines created by drift tube combinations (c). Ambiguous Lines 51
4.5 Cluster algorithm flow diagram 52
4.6 Selection of points for the draft χ^2 fit 53
4.7 Diagram of the main classes of the algorithm and flow control. 54
4.8 Performance results for single track events. Histograms (a), (b), (c) present the differences between the Monte Carlo and the reconstructed events of the values of the slope angle, offset, and the residuals respectively. The residual error (resolution of the track reconstruction) is 3.26 ± 0.03 μm. The next three histograms (d), (e), (f) show the same parameters with an applied smearing of 100 μm to each hit. The standard deviation of the fit in histogram (f) is 88.09 ± 0.50 μm. In graph (g), the correlation between the Monte Carlo generated radii and the reconstructed ones with a smearing of 100 μm is plotted. In graph (h), the residual error in μm versus the smearing in μm, for smearing factors up to 300 μm is plotted. Finally, in graph (i), the resolution versus noise using hits with a smearing factor of 100 μm is plotted. The data are simulated with noise up to 600%. 55
4.9 Reconstruction efficiency and fake rate as a function of noise level . . 56
4.10 (a) Size of the Legendre histogram space in memory, (b) Execution time of the algorithm, as a function of noise level 56
4.11 Examples of two track separation in noisy conditions and the corresponding Legendre transforms 57

5.1 (a) Difference in the R coordinate of the segment and the simulated track. (b) Difference in the z coordinate of the segment and the reconstructed track. (c) Difference in the θ angle between the segment and the simulated track (c) Residuals 61
5.2 (a). Matched reconstructed segments per event (b) Number of fake segments per event (c) Number of hits on segment for matched segments (d) number of hits on segment for fake segments. 62
5.3 Cavern background studies (a) Number of fake segments per event (b) Number of hits on segment for matched segments (e) number of hits on segment for fake segments. 64
5.4 Computing performance studies (a) Algorithm processing time (b) Histogram size in memory 67

List of Tables

2.1 Summary of the nominal MDT operating point. 12
2.2 Specification of tube and wire material and dimensions. 12

3.1 Properties of the Legendre transform. The $(df/dx)^{-1}$ denotes the inverse derivative of $f(x)$. 29

5.1 Muon data samples used in the analysis 60
5.2 Segment reconstruction efficiency for all algorithms 66
5.3 Segment reconstruction purity for all algorithms 66

Acknowledgments

First of all I would like to thank professors Theo Alexopoulos and Yorgos Tsipolitis for everything I have learned and for providing me the chance to work with them in the ATLAS experiment during the last two years. I had a great time with them both in CERN and NTU. I will never forget the fun we had in the office and in the lab! I will also never forget the very nice time we had at Geneva. All the work I took part in CERN during the last two years including BIS chamber installation, the MDT power supply slow control system and the muon reconstruction algorithm described in this thesis was a great research opportunity for me and very valuable for my next steps. I would also like to thank Dr. Sotiris Vlachos for all the precious advice and lessons while I was working with him in MDT installation and comissioning. For this thesis work I would also like to thank Niels Van Eldik, Jochem Snuverink and Peter Kluit for their help in developing the Legendre algorithm inside the ATLAS software framework (Chapter 5) and for providing me help with the segment comparison software so that I could provide comparison results with the other reconstruction algorithms. I would like to thank my friends Panos and Kostas for the nice time we had all these years I was in Athens.

To Maria for her love,
interest and understanding..

Chapter 1

The ATLAS Detector

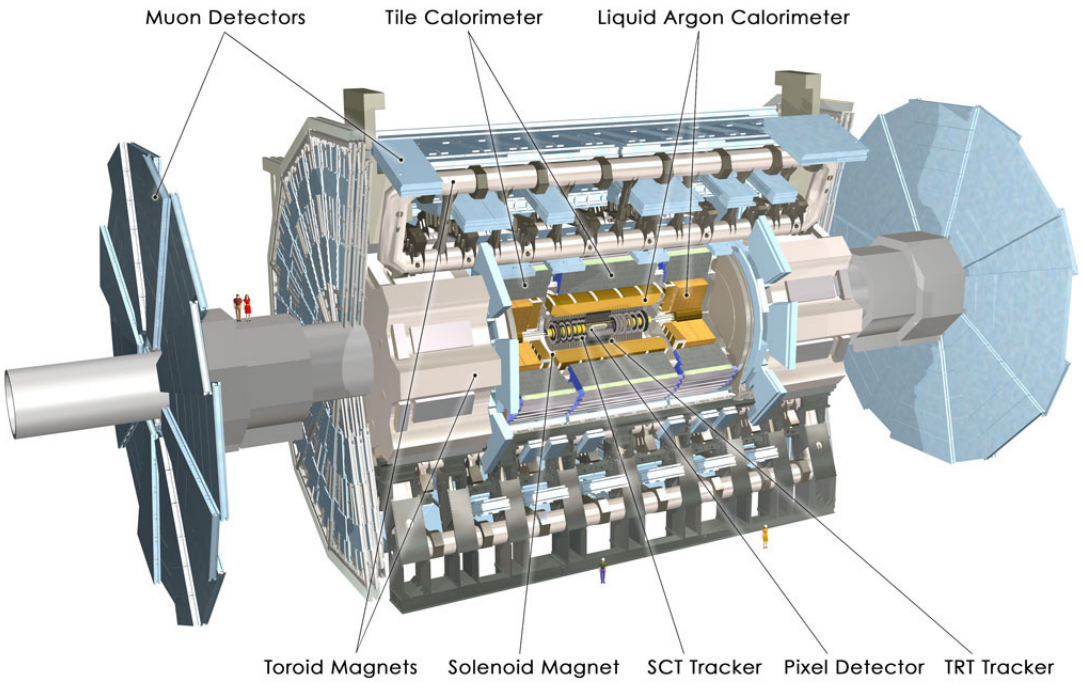

Figure 1.1: The ATLAS experiment

The ATLAS[4] (A Toroidal LHC Apparatus) detector is a general purpose experiment, designed to study new physics provided by the LHC in the energy frontier. The experiment is designed in common sense of the High Energy physics experiments of the last 30 years. A three-dimensional view of the detector is depicted in figure 1.1. It consists of the following main systems:

- Inner Detector

- Calorimeters
- Muon Spectrometer
- Magnet System

The inner detector[5] is located around the interaction region. It consists of the Pixel detector, the Silicon Tracker and the Transition radiation tracker and it is designed for accurate measurement of the position, sign and momentum of charged particles. For this reason, the inner detector is located inside a solenoid magnet which provides a homogeneous magnetic field of 2 T. Outside the Inner detector we have the electromagnetic and hadronic calorimeters[6] that measure the energy deposit by the particles that escape the inner region.
The outermost and largest part of the detector consists of the Muon spectrometer[7]. The muon spectrometer of ATLAS is a standalone system that can provide accurate transverse momentum (p_t) measurements. It consists of three toroidal magnetic systems that provide a mean magnetic field of 0.5 T. There are three layers of precision and trigger chambers measuring the curved tracks of the outgoing muons. The next sections describe the corresponding subsystems.

1.1 The Atlas Coordinate System

The ATLAS coordinate system is described in Fig. 1.2. The x axis points to the center of the accelerator tunnel while the y axis is pointing upwards. The z axis points towards the beam. Using cylindrical coordinates, the azimuthial angle ϕ is defined by the positive x axis and the polar angle θ corresponds to the positive y axis. The commonly used pseudo-rapidity $\eta$is used instead of θ and it is defined by:

$$\eta = -\ln\left[\tan\left(\frac{\theta}{2}\right)\right]$$

1.2 Inner Detector

The ATLAS inner detector is the heart of the apparatus. It consists of three subsystems contained in a 2 T solenoid magnet. The pixel detector is the first detector next to the interaction point. It consists of eight million pixels situated in three layers concentric to the beam line. The granularity is described by one pixel for each 50 μm in the transverse r, ϕ plane and one pixel per 400 μm for the estimation of the z coordinate of the interaction point. The pixel detector provides very accurate measurements of the three coordinates of the particle track (r, ϕ, z) which provides a high efficiency in resolving the interaction vertex. The next detecting layer of the inner detector is the Semiconductor Tracker (SCT). The barrel part consists

of four layers of silicon strips with a strip pitch of 80 μm. The strips in different layers differ by a stereo angle which can provide a z measurement. The end-cap parts are discs consisting of strips pointing the beam axis that provide the transverse measurement. In the same manner to the barrel part, the disc strips are situated in a small stereo angle for the possibility of a z measurement. The final part is the Transition Radiation Tracker (TRT). The TRT is a straw type drift detector similar to the Muon Drift tube chambers but much smaller. The drift straw maximum length is 150 cm and the radius is 4 mm. The straws are aligned parrel to the beam axis to provide measurements of the bending tracks. The TRT can also detect transition radiation. Transition radiation is emitted when a relativistic particle passes through the border of two media with different electrical properties. The transition radiation can provide information about the velocity of the charged particles. This is important for separating different particles like electrons from pions. Summarizing, the ATLAS inner detector is designed to provide accurate measurements in the LHC high density environment. The data rate is estimated to be 40 MHz and the detector must detect the particles coming from the event in less that the 25 ns of the bunch crossing to reduce particles coming from previous events. The typical momentum resolution of the ATLAS inner detector is $\Delta p_t/p_t = 0.04\%$ and the resolution of the space measurements in the transverse plane is 15 μm.

1.3 Calorimetry

The ATLAS calorimeter system consists of the electromagnetic and the hadronic calorimeter. The electromagnetic calorimeter uses lead as absorber and liquid argon as the sampling material. The geometrical coverage is defined by $|\eta| < 3.2$ and $0 < \phi < 2\pi$. For $|\eta| < 2.5$ there are three calorimeter sections whereas for higher rapidities there are only two. The width of the calorimeter is more than 24 iteraction lengths providing that most of the particles will be measured. The energy resolution of the liquid argon calorimeter is:

$$\frac{\Delta E}{E} = \frac{11.5\%}{\sqrt{E}}$$

where E is measured in GeV and the polar angle resolution is

$$\Delta\theta = \frac{50 \text{ mrad}}{\sqrt{E}}$$

The hadronic part consists of iron tiles in the barrel and liquid argon in the end-cap. In the barrel region, the tiles are interleaved by scintilators. The end-cap part consists of liquid argon. The average jet resolution of the calorimeter is

$$\frac{\Delta E}{E} = \frac{50\%}{\sqrt{E}}$$

Finally, the last - forward part of the hadronic calorimeter consists of three layers.The first is made of cooper and the other two are made of tungsten. All layers use liquid argon as sampling material.

1.4 Muon Spectrometer

The Muon Spectrometer is the largest sub-detector in the ATLAS apparatus. In most of the pseudorapitidy range, it consists of three detecting layers filled with trigger and precision chambers. The Muon spectrometer has been designed with the capability of a standalone operation. There is a standalone trigger and the momentum can be measured with high accuracy.

For bending the tracks, three large toroid magnets consisting of eight coils are used (Fig 1.3.c). In the barrel region, the large barrel toroid magnet covers a large area of 25 m length and five meters radius with inner radius of 4.7 m and outer radius of 10 m. The two end-cap toroids have a length of 5 m and a diameter of 10.7 m. They also consist of eight coils radially configured. The magnet system provides an average bending power of 3 Tm in the barrel and 6 Tm in the end-cap. The magnetic field map has an eightfold shape because of the finite number of toroid coils (Fig 1.3.b) and the bending power becomes lower in the transition region between the barrel and the end-cap because of the superposition of the fields.

1.4.1 Muon subdetectors

The barrel part of the Muon Spectrometer consists of three layers of subdetectors. The inner layer consists of Monitored Drift Tube (MDT) chambers. These chambers (named BIS, BIL) are positioned outside the calorimeter. They are triggered by the LHC clock and can provide accurate measurements of the trajectories of the muons. The MDT chambers consist of aluminum tubes and detect particles by the drift of the electrons produced by ionization of gas atoms. The MDT chambers are described in detail in the next chapter. The MDT chambers of the middle layers (BML, BMS, BMF) are surrounded by two trigger chambers on each side, the Resistive plate chambers (RPC). The trigger chambers provide trigger information and measurement of the second coordinate of the particle tracks. The middle layer detectors are placed inside the magnet. Finally the third layer consists of MDT chambers (BOF, BOS, BOL) paired with an RPC in the outer surface.

The end-cap scheme is different because it is impossible to install chambers inside the end-cap toroids. The first layer of end-cap detectors is placed outside the magnet . These detectors are Cathode strip chambers (CSC) that provide accurate measurements at higher rates than the MDT and this is the reason they are stationed in this region. The middle and outer layers consists of MDT chambers. The trigger chambers used in the End-cap are Thin gap chambers (TGC) and are placed on both

sides of the middle MDT layer. A three dimensional view of the different detector layers in barrel and end-cap region is depicted in Fig.1.4.

1.4.2 Muon Reconstruction

For the reconstruction of muons in ATLAS, the Muon spectrometer can be used for identification and/or measurement while the inner detector is used for measurement of the charged particles . There are two different types of reconstruction:

- Combined Reconstruction (Muon spectrometer + Inner detector)
- Muon Spectrometer standalone reconstruction

In the second case it is also possible to provide an energy correction to the muon spectrometer reconstructed tracks. The correction is referring to the reconstruction of the muon energy reconstructed in the calorimeter. The transverse momentum(p_t) measurement of the particle in the Muon spectrometer is taking place on the rz plane where the bending power of the magnets is present. In the r, ϕ plane the tracks are straight lines. The monitored drift tubes are vertical to the beam axis to measure the curved tracks. However inside a chamber, the curvature of the track can be neglected and the tracks can be considered as straight lines. The typical steps of the reconstruction in the muon spectrometer are outlined below.

- Search of particle patterns in the bending and non bending plane and merging to roads.
- Local Segment reconstruction for the precision detectors.
- Association of segments to roads and fit of the track.
- Material corrections.

The first step is done with the trigger hits. Particle roads are found in the bending and non-bending plane and the patterns are combined to form global roads. Segments reconstructed in the local detector sections are associated to roads to form particle tracks. Finally tracks are fitted for extracting the momentum. Some material corrections are applied. The second step (Segment reconstruction) is the main topic of this thesis and is described in the following chapters.

Muon reconstruction algorithms

The arsenal of the reconstruction algorithms in the ATLAS Muon spectrometer is very large. There are four full reconstruction packages:

- Moore[15] (Muon object oriented reconstruction) written in C++.

- Muonboy[16] written in g77.
- MuGirl (C++).
- MoMu (Modular muon reconstruction) written in C++ in a completely modular approach.

1.4.3 Performance of Muon Spectrometer

A typical study of the performance of the Muon Spectrometer is presented in this section. This study was performed with GEANT Monte Carlo events in the ATLAS software framework using the Moore package. The latest version of the algorithms has been used. A sample of 300 K events with top decays in the lepton+jet channel was used for the study. The muons produced by the W decay of top have an average transverse momentum of 40 GeV and they are ideal for performance measurements. The results of the analysis are presented in Fig. 1.5. The first column shows the reconstruction efficiency of the detector as a function of the transverse momentum (a), the pseudo-rapidity η (c) and the azimuthial angle ϕ (e). In all plots the standalone reconstruction is compared to the combined reconstruction. It can be concluded that the acceptance in the standalone operation is larger than in the combined one. This is expected because in the combined case there is a match between the muon spectrometer and the inner detector tracks. The difference in the efficiency refers to the cases where this match has not been done. Fig. 1.5.a shows a very smooth behavior of the detector in the the p_t spectrum. In Fig. 1.5.c, there are some regions where the efficiency is low. In $\eta = 0$ there is a gap between the muon chambers where cabling services of the muon spectrometer are installed. In $\eta = \pm 1$ there is the transition region between the barrel and the end-cap where the bending power is much lower and the tracks may pass through less than three layers of chambers. In Fig. 1.5.e we have a smooth behavior of the efficiency vs ϕ except two regions in negative ϕ which correspond to the supports (feet) of the detector.

The second column contains measurements of the resolution of the Muon spectrometer. In Fig.1.5.b the resolution in transverse momentum is plotted. This plot explains all the effort for the creation of the ATLAS Muon spectrometer. The standalone measurement of p_t for the Muon spectrometer is very near to the combined (Tracker and Muon) measurement. Tracker provides very higher granularity and in this p_t region, there is a detectable curvature of the track inside the tracker which results in a very accurate measurement. In very higher p_t samples, the Muon spectrometer dominates in the Muon measurement. From Figures 1.5.c 1.5.f it can be extracted that the muon spectrometer efficiency in deriving the impact parameter coordinates is much lower that the inner detector, something that is expected because of the large area the spectrometer covers and the tracking resolution of the precision chambers.

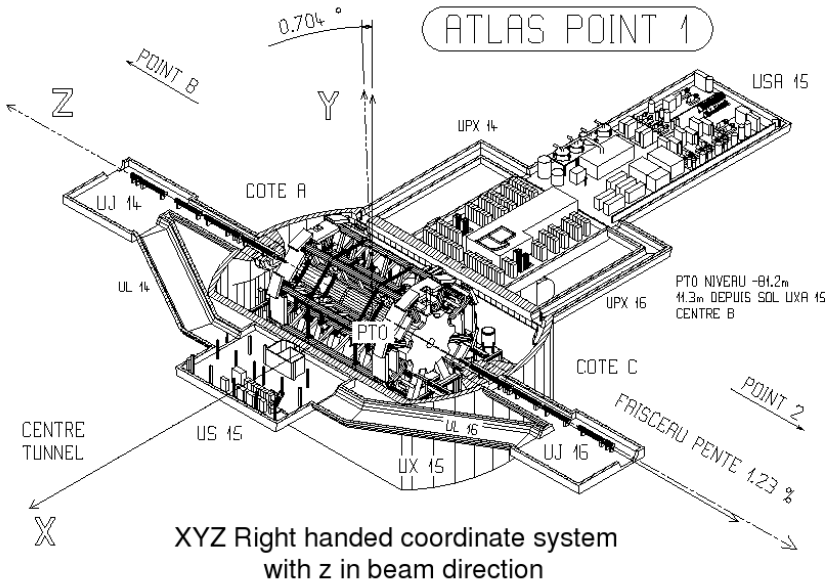

Figure 1.2: The ATLAS coordinate system

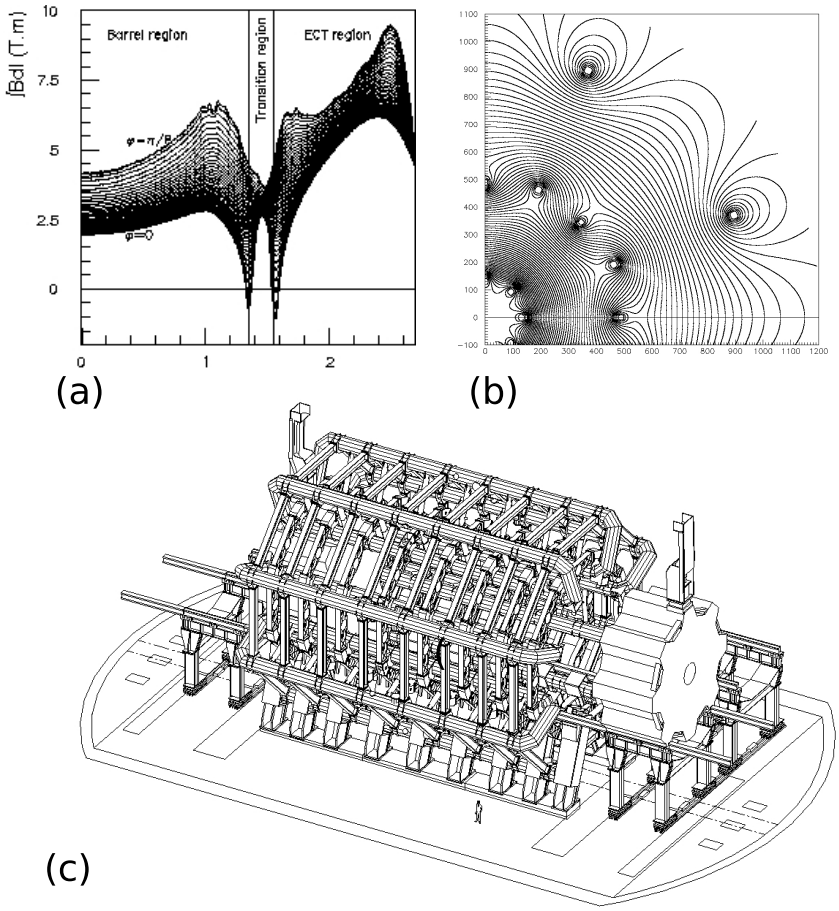

Figure 1.3: ATLAS Toroid magnets. (a) Bending power in the barrel, end-cap and transition region (b) Magnetic field map lines in the transverse plane (transition region) (c) Atlas Barrel end end-cap toroid instrumentation

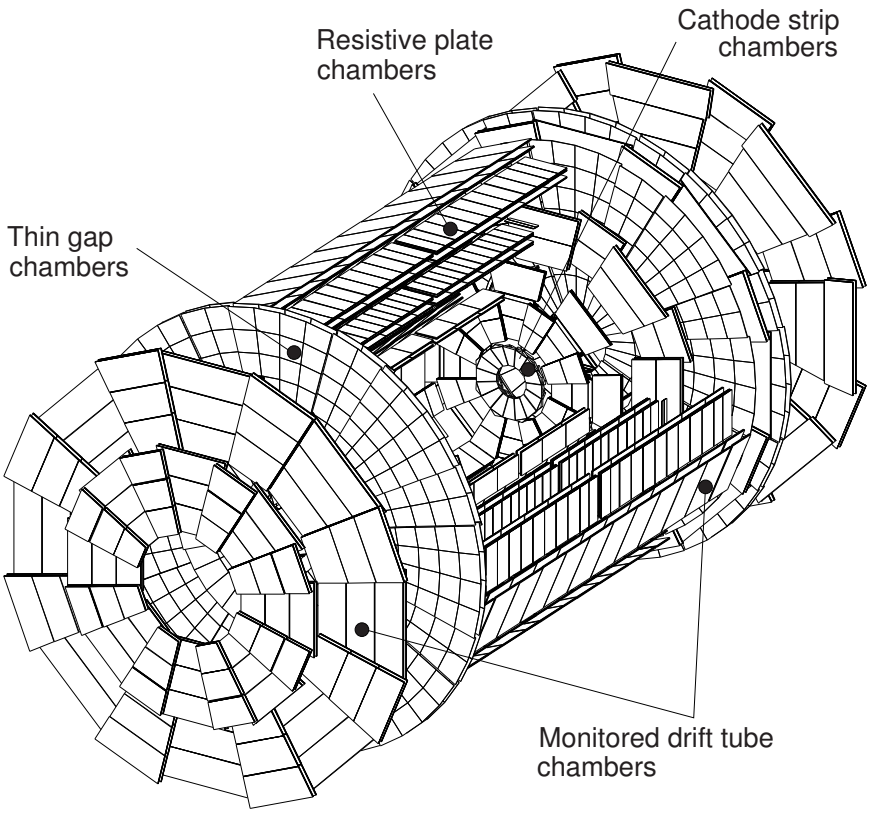

Figure 1.4: Muon instrumentation of the ATLAS experiment

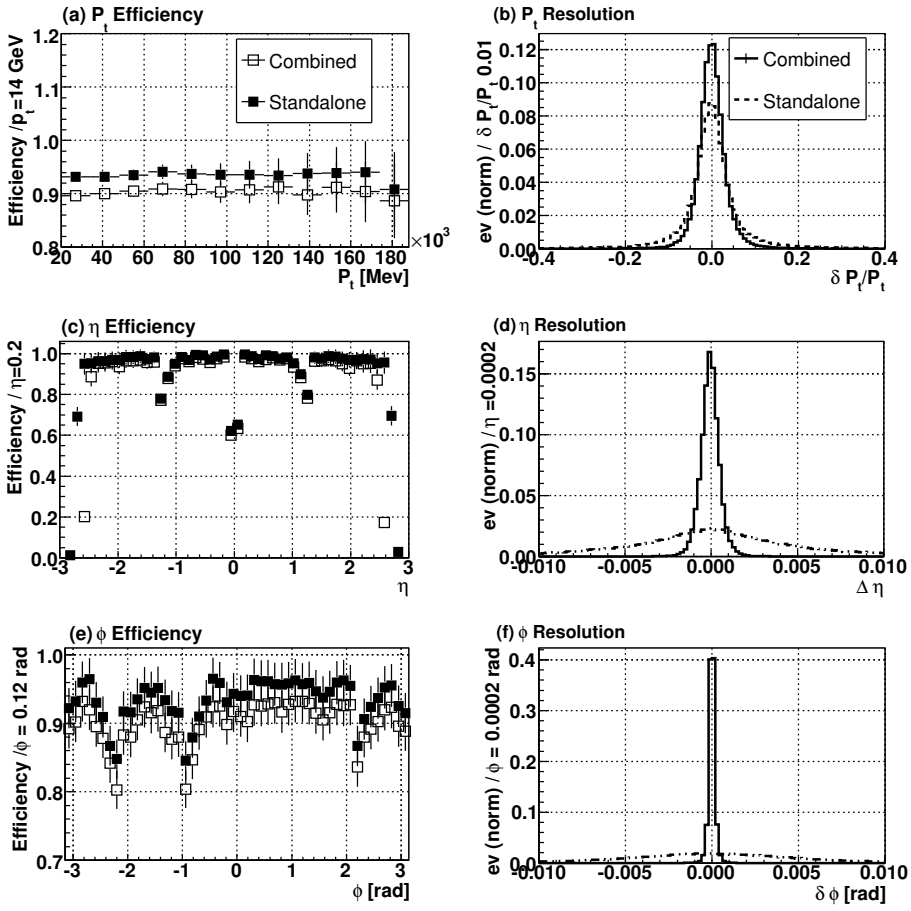

Figure 1.5: Muon Reconstruction efficiency for combined and standalone reconstruction. (a) Efficiency vs p_t. (b) p_t resolution. (c) Efficiency vs η. (d) η resolution. (e) Efficiency vs ϕ. (f) ϕ esolution.

Chapter 2

MDT Chamber Physics and Technology

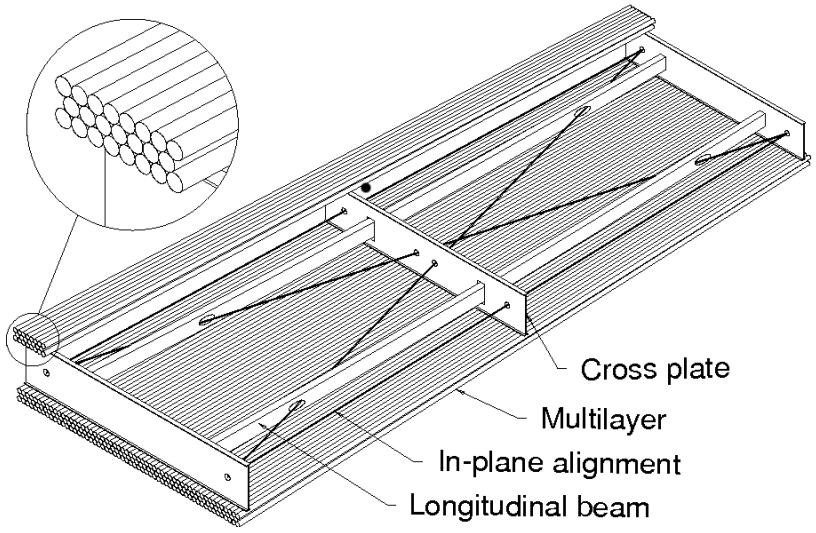

Figure 2.1: A Monitored Drift Tube chamber

Drift chambers are well known and commonly used instruments for charged particle detection(especially muons) in High Energy Physics experiments. A typical drift chamber is considered as a closed gas-filled space containing signal wires. The ATLAS MDT chambers (acronym for Monitored Drift Tube) consist of individual drift tubes and perform the precision coordinate measurement in the bending r, z plane of the air-core toroidal magnet to provide accurate transverse momentum measurements. The ATLAS MDT system covers the entire area of 5500 m^2 consisting of three layers of detectors that cover a pseudorapidity range of $-2.7 < \eta < 2.7$. The basic detection element of the Monitored Drift Tube Chamber is a cylindrical aluminium drift tube

of a diameter of 30 mm and a W-Re central wire with a diameter of 50μm. It is operated with nonflammable gas composed of $Ar(90\%)$, $CO_2(10\%)$, at 3 bar absolute pressure for reduced diffusion and ionization fluctuations. The wire is held at a potential of +3080 V with reference to the grounded tube. The amplification factor is set to be very low, $2 \cdot 10^4$, to minimize the effect of ageing. The operating point is summarized in Table 2. The drift tubes consist of the tube, the wire and the endplug.

Table 2.1: Summary of the nominal MDT operating point.

Parameter	**Design value**
Gas mixture	Ar(90%), CO_2(10%)
Gas pressure	3 bar absolute
Gas gain	$2 \cdot 10^4$
Wire potential	3080V
Maximal drift time	1200ns
Effective threshold	22nd electron
Resolution	$80\mu m$

The specifications (taken as engineering tolerances) are $30.000^{+0.000}_{-0.030}$ mm for the tube outer diameter and 400 ± 20 mm for the wall thickness. Some parameters about tube specifications are summarized in Table 2.

A W-Re (97/34) gold-plated (3% by weight) wire is used for the anodes of the drift tubes with diameter 50.0 ± 0.5 μm . The 3% rhenium admixture increases the rupture limit to 620 g, which is higher than the diesigned wire tension of 350 g. The rhenium also facilitates the handling of the wire. These parameters are summarized in table 2.

Table 2.2: Specification of tube and wire material and dimensions.

Tube		**Wire**	
Parameter	**Design value**	**Parameter**	**Design value**
Material	Aluminium	Material	W/Re - 97 : 3
Density	2.73g/cm^3	Density	19.3g/cm^3
Outer diameter	$30.000^{+0.000}_{-0.030}$mm	Diameter	50.0 ± 0.5mm
Wall thickness	400 ± 20mm	Surface coating	gold-plated 3% by weight
Length	$\pm$0.5mm	Rupture limit	620g

Finally the endplugs are considered as the key components regarding the electromechanical drift tube characteristics. They are responsible for position the wires precisely with respect to the tube walls, make the electrical contact between front-end electronics and between wire and front-end electronics and tube wall, hold the me-

chanical wire tension and make the gas seal and the connections to the on-chamber gas manifold.

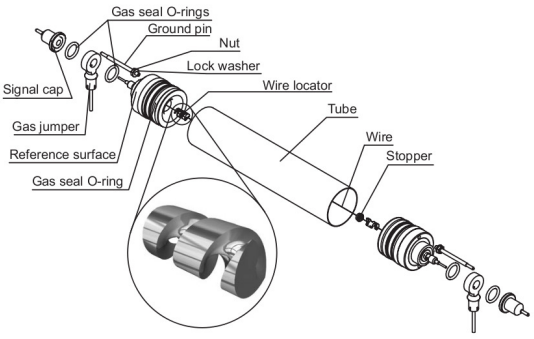

Figure 2.2: Monitored Drift tube and endplug

A Monitored Drift Tube Chamber is an assembly of parallel layers $(3, 6, 8)$ of drift tubes on a frame. Each chamber can have one or two multi-layers with three or four layers of tubes on each side. The tubes with their diameter of 30 mm are closely spaced so that a layer of three tubes has a thickness of about 82 mm. The Monitored Drift Tube Chambers closest to the interaction point have been equipped with four layers of tubes per multi-layer to optimize the pattern recognition performance at high background rates. By measuring the drift time of the ionization electrons in the gas, one determines (maximum) six coordinates of a typical track in the plane of the layer and in the direction across the tubes. This results in a measurement of effectively one coordinate with 80 μ m precision. Local segments play an important role for track reconstruction and in the calibration of a MDT chamber. To ensure accurate local reconstruction of segments within one MDT chamber, several devices are locally installed in order to monitor the operation conditions of the chamber:

- Temperature and magnetic field sensors installed on the chambers ensure accurate knowledge of the local environment. The precision on the magnetic field is $\Delta B/B = 4 \cdot 10^4$ and on the temperature $\Delta T = 0.5$K;
- All MDT chambers are equipped with an in-plane RASNIK alignment system which measures the dominant modes of the chamber deformation with a precision of 20 μm ;
- The chambers were constructed with a mechanical precision better than 20 μm .

2.1 Physics of drift tube chambers

The detection of particles and photons is based on their interaction with the medium of the detector. A charged particle passing through a material interacts via electromagnetic forces with electrons ,nuclei and the medium as a whole. As the result of these interactions, the charge particle loses energy, changes its direction and finally stops after traveling a finite distance called range. Most of the energy losses refer to molecule and atom excitation and ionization. The possible energy loss mechanisms are:

- Coulomb interactions with electrons and nuclei
  - atom excitation
  - atom ionisation
- Electromagnetic radiation emission called bremsstrahlung (emitted in deceleration of particle in Coulomb field)
- Nuclear interactions
- Cherenkov radiation emission (above certain threshold and if medium is transparent)
- Electromagnetic radiation emission called transition radiation (emitted in traversing a medium with discontinuous dielectric constant).

Coulomb interactions dominate for the gas medium of the Monitored Drift Tube Chambers. Since the radius of the nucleus is approximately $R_1 = 10^{-14}$ m and the radius of the atom is $R_2 = 10^{-10}$ m one expects that:

$$\frac{\text{number of interactions with electron}}{\text{number of interaction with nuclei}} = \frac{{R_2}^2}{{R_1}^2} = 10^8$$

This simple model shows that collisions with atomic electrons are much more probable than collisions with nuclei.
Atom Excitation takes place when atomic electrons acquire enough energy to move to higher energy levels than the ground state $E_1 \longrightarrow E_2$ to create an excited atom. When electrons fall back to their original orbit, they emit characteristic X-ray photons with energy $\Delta E = E_2 - E_1$.
Atom ionization takes place when atomic electron obtains enough energy to leave the atom and become a free electron with kinetic energy: $E = E_{acq} - I_{ion}$ where E_{acq} is the energy acquired from the particle and I_{ion} is the ionization potential. Liberated electrons act as independent particles. If their energy is high enough, they can cause further ionizations. Those are called δ electrons. For noble gases the cross-section is about 10^7 barn , so the possibility to produce ions and electrons in a noble gas is limited. However, it is possible for the excited atom to take part to additional reactions that finally can lead to ionization.

Another mechanism of ionization caused by the Penning effect. In some molecules or atoms, metastable electrons that do not fall back directly to the ground state, are able to de-exitate by a collision with another atom which leads to ionization of the second atom:

$$\mathrm{Ne^* + Ar \rightarrow Ne + Ar^+ + e^-}$$

For noble gases, one pair of ion-electron is produced on average for every 30 eV of energy that the passing charged particle loses. For example, if the incoming particle

has 3 keV energy and losses all of his energy in the gas volume, 100 pairs of ions-electrons will be produced.

In the presence of an external electric field the electrons are recombined with the ions (because of their electric attraction) emitting a photon:

$$\mathrm{X}^+ + \mathrm{e}^- \rightarrow \mathrm{X} + \mathrm{h}\nu$$

It is also possible for two ions to recombine:

$$\mathrm{X}^- + \mathrm{Y}^+ \rightarrow \mathrm{XY} + \mathrm{h}\nu$$

In general, the recombination rate n depends on the concentration of the positive and negative charge cariiers n^+, n^- respectively. The electron capture procedure is based on the captivity of free electrons from electronegative atoms forming negative charged ions:

$$\mathrm{e}^- + \mathrm{X} \rightarrow \mathrm{X}^- + \mathrm{h}\nu$$

. This kind of atoms have their external shell almost full, so adding one more electron leads to liberation of energy. The negative ion that is formed is unstable. That leads us to the conclusion that the choice of electronegative gas in the detector will dramatically reduce the performance of it, because the electrons will be captured in the detector before they give a signal response.

Charges produced by ionizing events quickly lose their energy in multiple collisions with the gas molecules and finally recombine. The average value of the thermal energy of the molecules is derived by simple kinetic theory as: $\varepsilon T = 3/2kT = 0.04\mathrm{eV}$ (stp). The velocity distribution for the charged particles with the average thermal energy is provided by the Maxwell distribution. The average velocity is

$$U = \sqrt{\frac{8kT}{\pi m}}.$$

It is denoted that for the same temperature, the average velocity for ions is smaller than the average velocity of electrons because of their great difference in masses. In room temperature (20^oC) the thermal velocity of electrons is about 10^4m/s while ions have almost 10^2m/s. The relation between the number of charged particles, N, and the position, x, after an interval time t is

$$\frac{dN}{dx} = \frac{N_0}{\sqrt{4\pi Dt}} \exp \frac{-x^2}{4Dt}$$

where N_0 is the total number of charged particles, x the spatial coordinate in the system with the creation point of the particles as the origin and D the diffusion coefficient. The rms is given from $\sigma(x) = \sqrt{2Dx}$ and if instead of x the spherical coordinate r ($r = |\vec{r}| = \sqrt{x^2 + y^2 + z^2}$) is used, the volume diffusion can be defined ($\sigma(r) = \sqrt{6Dr}$). The volume diffusion of ions in the air under stp is approximately

10^{-3} m after an interval time of $1/s$. The diffusion coefficient is provided from kinetic theory as $D = u\lambda/3$ where λ is the mean free path between collisions. For classical ideal gas:

$$\lambda = \frac{1}{\sqrt{2}}\frac{kT}{\sigma_0 p}$$

where σ_0 is the total cross-section. One can deduce the following expression for the D:

$$D = \frac{2}{3\sqrt{2\pi}}\frac{1}{\sigma_0 p}\sqrt{\frac{(kT)^3}{m}}$$

.

When an external electric field is applied across the gas volume, the electrons are moving towards the cathode and the ions towards the anode. Because of the collisions with the molecules of the gas, the electrons achieve almost spontaneously an average drift velocity. The last one is added to the thermal velocity. The mobility is given by $\mu = \frac{u}{E}$ where u is the drift velocity and E the electric field. For moving charged particles across an ideal gas in the average thermal energy distribution of the gas,Einstein's formula can be used:

$$\frac{D}{\mu} = \frac{kT}{e}.$$

It is possible to achieve a drift velocity of the order of 10^6 m/s before the saturation point. In this range of velocities, the external electric field is almost 1 kV/cm. The diffusion coefficient D increases and leads to greater diffusion of electrons. With the presence of a magnetic field H via the Lorentz force, the drift velocity changes. The magnitude of the new drift velocity is

$$u_{d,H} = \frac{u_d}{\sqrt{1+\omega^2 t^2}}$$

where $\omega = eH/m$ and the angle that the new vector of velocity creates with the electric field lines is $a_H = \arctan(\omega t)$. The electrons from primary ionizations caused by the incoming particle, are able to further ionise the gas (if they gain enouph energy). The second generation of electrons are also able through the same process to repeat the ionization process. Finally, multiple produced pairs are created. This phenomenon takes place in the area very close the cathode (typical distances of nm). In this region, the electric field reaches great values because of the inverse relationship with the distance($E \approx 1/r$). The electrons have greater mobility than ions therefore the avalanche shape is like a drop of water. The fast electrons are responsible for the front part of the drop and the heaver and slower ions form the tail of the drop.

The possibility of ionization per unit length is given by $\alpha = 1/\lambda$, where λ is the mean free path between collisions that leads to ionization. This is also called Townsend

coefficient. If n is the number of electrons at a given position, after a path dx, the increase in their number will be $dn = n\alpha dx$ and by integration

$$n = n_0 e^{\alpha x}.$$

The multiplication factor M can be defined by $M = \frac{n}{n_0} = e^{\alpha x}$. In a case of a non-uniform electric field where $\alpha = \alpha(x)$, the previous relation has to be modified in the following way:

$$M = \exp \int_{a_1}^{a_2} \alpha(x) dx.$$

The multiplication factor cannot be increased at will. Secondary processes, like photon emission can induce the generation of avalanches and space-charge deformation of the electric field which is strongly increased near the front of the avalanche . These eventually which result in a spark breakdown. Finally, for a cylindrical detector the Diethorn equation can be used:

$$ln(M) = \frac{ln(2)}{\Delta V} \frac{V}{\ln \frac{b}{\alpha}} \left(\ln \left(\frac{V}{p\alpha \ln \frac{b}{\alpha}} \right) - \ln K \right)$$

where M is the gas multiplication factor;

V is the applied voltage

ΔV is the potential difference through which an electron moves between successive ionizing events

α is the anode radius

b is the cathode radius

p is the gas pressure

K represents the minimum value of E/p below which the multiplication cannot occur.

The primary amount of electrons is not capable of efficient detection. The solution for that is to amplify our signal via the avalanche in a proper gas mixture that contains a noble gas. Typical noble gases, which have low ionizing potential, are Ar, Kr and Xe. A detector with only Ar as a gas is not possible to provide a gain greater than $10^3, 10^4$. This was denoted as a result of the behavior of the excited noble gas. The noble gases that are usually used de-exitate, emitting a photon with more energy than the ionization potential of the metal that is usually used inside the detector. For the Ar, the energy of the photon is 11.6 eV. If the selected metal has a work function of the order of this energy (and lower), photoelectric effect can occur.

The electrons extracted from photoelectric processes act as the electrons from primary ionizations, and finally create avalanches and provide fake pulses. In order to avoid this phenomenon a quantity of a polyatomic gas can also be induced into the detector. The molecules of polyatomic gases (i.e. CO_2) have a lot of degrees of freedom,

(rotations, oscillations) which results to a broad spectrum of energy levels. In other words, the molecule can be exitated in many different ways so it can absorb a great quantity of energetic photons without de-exitations and production of photons (i.e. methane CH_4 can absorb photons with energy starting from 7.9 eV to 14.5 eV). This process is called quenching and with that we are able to use noble gases to detectors with gain up to 10^6. However the usage of polyatomic gas to the detector leads to some unpleasant chemicals processes which causes a decrease to the gas density. In order to overcome this purification and recycling of the gas is needed.

2.1.1 MDT Operation in ATLAS

A charged particle crossing the tubes interacts via the electro-magnetic force with the gas. As we have already described, along the trajectory of the particle the gas will be ionized and excited. The free electrons produced by ionization start to drift towards to the wire and generate a signal. In the vicinity of the wire, the electrons obtain sufficient kinetic energy due to the high electric field close to the wire and trigger the main avalanche process. The drifting electrons gain energy, high enough to ionize further gas atoms and create more electron-ion pairs. The electrons released here also gain enough energy for further ionization. The whole procedure results in a signal amplification, the gas gain. The amount of charge produced in the avalanche is typically six orders higher than the amount originally produced by the incoming particle (primary ionization). The signal on the wire propagates to the end of the tube, where a current-sensitive amplifier and shaper (15ns peaking time) followed by a discriminator feeds a timing pulse into the on-chamber time-to-digital converter (TDC). The amplification factor M depends on the gas, gas density and electrical field. The charge induced to the wire is enough to be detected by on-chamber electronics. In order to get information about the position of the particle, it is necessary to measure the time the electrons needed to drift from the origin point on the particle track to the wire. This time is correlated with the minimum distance of the particle track to the wire. This is the so-called $r - t$ relation. The r-t relation is used in order to translate the drift time information into the radial distance, where the particle was crossing the tube. While the arrival time of the electrons at the wire can be determined by the electronics connected to the wire, the time of the particle traversal has to be determined by an additional trigger detector close to the drift tubes. For the determination of the particle track, a combination of several drift tubes is needed. The combination of all distances between the particle track and the wires enables the reconstruction of the track in the coordinate perpendicular to the wire.

Figure 2.3: Drift tube operation in a magnetic field with curved drift path.

2.2 Construction imperfections and ageing

In this section, some very important issues affecting the imperfections adn ageing of the monitored drift tube chambers are selected.

2.2.1 Displacement of the wire

Displacement of the central wire can occur due to the gravitational force or partial mechanical failure of the wire supporting part of the endplug. Due to the gravitational force, the wires in the tubes are not straight but follow a parabolic curve given by the equation:

$$s(x) = \left(1 - 4\frac{x^2}{L^2}\right) \cdot \left(\frac{\pi\rho R^2}{8T}\right) \cos(\phi).$$

where x is the distance from the tube center, $s(x)$ is the wire displacement, L is the tube length, ρ is the wire density ($g \cdot \mathrm{cm}^{-3}$), R is the wire radius, T is the wire tension (g) and ϕ is the azimuthal angle of the chamber (all lengths). This has some consequences on reconstruction and on operation conditions. During reconstruction if the wire is displaced and if the wire position is not corrected for the sagging of the wire, the calculation of the radial residual $\Delta r = |r_{track} - r_{drift}|$ would yield a wrong answer. As the functional shape of the wire and the wire tension and wire length are known with great precision, the actual wire position can be calculated during reconstruction. The fact that the wire is not perfectly centered in the tube deform the electric field in the tube and also change effectively the distance that electrons have to travel in order to reach the wire. As a result, the rt-relation is split into two parts: one for each side of the displaced wire. The barrel chambers are mechanically deformed such that the tubes follow the sag of the wire to ensure the non-concentricity of the wire is less than 100μ m. If not taken into account during reconstruction, the non-concentricity of the wire degrades the single tube resolution. The first-order approximation the shift of the rt-relation can be predicted by the formula

$$\delta r_{sag}(t) = \frac{2s}{r_{tube}^2} \cdot \cos(\phi) \cdot u_0(t) \int_0^t \left(\frac{u_0(t')}{u_0(t)} - 1\right) r_0(t')dt'$$

where $\delta r_{sag(t)}$ is the shift of the rt-relation (as a function of time), s is the displacement of the wire from the center of the tube, r_{tube} is the tube radius, ϕ is the angle with line through the wire and the tube center and $\nu_0(t)$ the derivative of the $r-t$-relation as a function of the time. If the $r-t$-relation is corrected using this formula the overall impact on the momentum resolution due to the non-concentricity of the wire is small. In the figure 2.4 we can see the deformation of the shape of the electrical drift field caused by wire displacement and also we can notice that the maximum value has change from 3kV to 1.6kV.

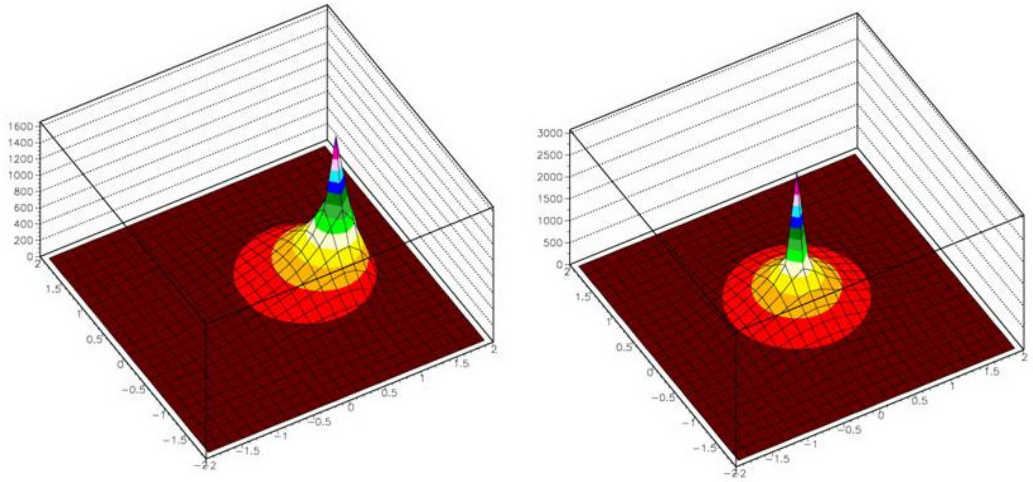

(a) Displaced (b) Centered

Figure 2.4: Shape of the electric field with and without displaced wire.

2.2.2 Ageing Processes

Ageing is usually caused by deposits on the anode and/or cathode. These deposits come into existence due to break up of gas molecules during normal operation of the chamber. These new molecules and radicals can form new non volatile molecules which then may stick to cathode or anode. There are four processes which can cause a breakup of the molecules within the gas:

1. Collisions with the traversing particles (least frequent).

   The traversing particle transmits energy during the collisions to the gas particles which can lead to ionization, excitation or fragmentation (in case of molecules).

2. Avalanche process.

   Since the energy of the electrons is sufficient to ionize atoms and molecules (typically 10 to 15 eV required) it is also sufficient to break the bond of molecules (typically 3 to 8 eV required).

3. Charge exchange.

   It takes place when an ion collides with a molecule or an atom, which has a lower ionization potential. Break up of chemical bonds dueto atomic charge exchange is possible when the difference in ionizations energy between the two species is larger than the binding energy.

4. Neutralization of the ions at the cathode.

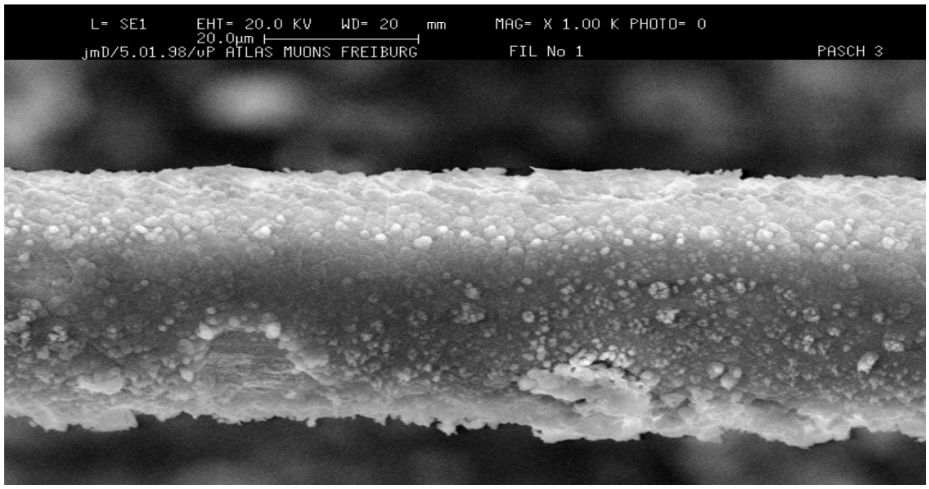

Figure 2.5: Picture taken with an electron microscope of a wire of a tube. The thickness of the layer is about 2μ m

This possibility depends on the energy difference of the work function of the surface and the ionization energy of the incoming molecule.

Polymerization of hydrocarbons is believed to be the major process leading to ageing of a drift chamber. Long polymers are non volatile and have a tendency to drift in the inhomogeneous drift field towards the wire due to their dipole moment. Hydrocarbons are usually found as a coating of the wire of aged tubes. Some products (solid or liquid) stick in the electrodes of the detector changing its behavior. This is also the main concept of the **Malter** effect. One very thin layer of insulating material is formed (mostly via polymerization) on the cathode causing the positive ions to settle on this layer and not to be absorbed on the cathode. The ions, in combination with the metal, create a very strong field because they are very close to each other. The thin layer of the insulating material has the thikness of some μm. This field is able to liberate some electrons from the surface of the cathode(reduces the work function) and therefore to create an avalanche and a false signal.

The sputtering technique enables both chamber reanimation as well as prevention of ageing. The basic idea is concentrated on ion bombardment of the deposits with a chemical reactive gas ($\mathrm{Ar}-\mathrm{O}_2/99-1$). This procedure is very effective and reliable in removing those non volatile hydrocarbons from the wire by forming volatile molecules like CO_2 and CO which were then completely removed from the tube by the gas flow. The ion bombardment is effective both at the wire and at the same at the tube wall. On the wall, the impurities are removed in an analog way as the deposits on the wire. This cleaning procedure for the tube wall has been prved to be the most effective of all. Thus sputtering can be used for prevention of ageing which is caused by impurities sticking at the tube wall.

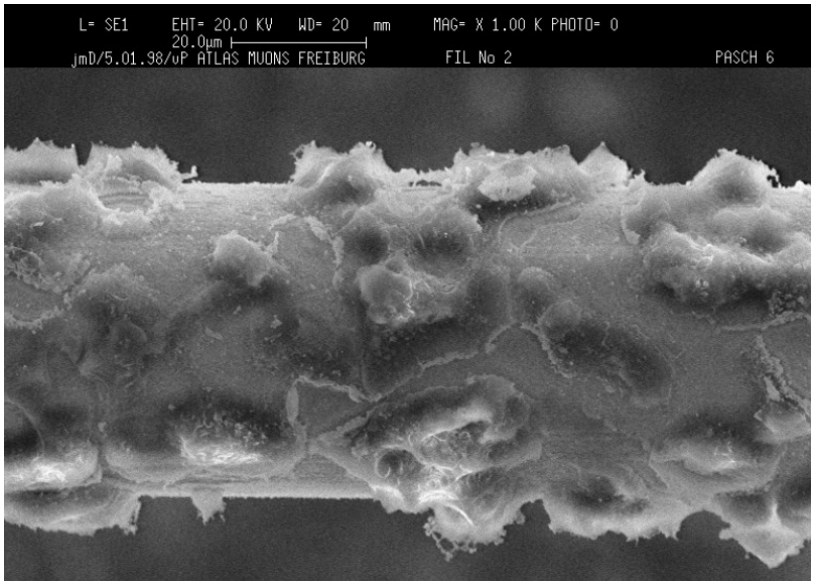

Figure 2.6: Wire partly reanimated using sputtering in pure argon. Some parts are still covered with a layer of carbon and oxygen, some parts show the gold layer of the wire. The average pulse charge of the wire at this state was about 75% compared to a new one.

Chapter 3

The Legendre Transform

The Legendre transform is a well-known mathematical tool in Thermodynamics and Analytical Mechanics formalism. In this chapter the Legendre transform and its basic properties are presented. The transform relation is generalized to be valid for both concave and convex functions. The study is concentrated to the geometrical properties of the transform as it transforms a function to all its tangent lines.

3.1 Definition

Consider a convex function $f\colon \mathcal{R} \to \mathcal{R}$ ($d^2f/dx^2 > 0$) and a straight line of the form $y = px + a$, where p and a are the slope and intercept, respectively. For a slope value p, the Legendre transform $F(p)$ of the function $f(x)$ is defined as follows [3, 1]:

$$F(p) = \sup_x \left[px - f(x)\right] = -\inf_x \left[f(x) - px\right].$$

The notation $\sup_x$ indicates the maximization of the function $px - f(x)$ with respect to x for constant p, while $\inf_x$ indicates the minimization of $f(x) - px$ with respect to x while p is held constant. The relationship between $f(x)$ and its Legendre transform is denoted by:

$$f(x) \overset{\mathcal{L}}{\longleftrightarrow} F(p).$$

Geometrically, the Legendre transform can be constructed in the following way (Fig. 3.1a): We plot the function $y = f(x)$ and for a given p we plot the line $y = px$. We take the point $x = x_0$ at which the curve $f(x)$ is farthest from the straight line in the vertical direction. The Legendre transform for the given p is given by $F(p) = px_0 - f(x_0)$. From Fig. 3.1, it can be derived that for a value of the slope p, a line $y = px - F(p)$ can be defined which is tangent to the curve $y = f(x)$. Thus each point $(p, F(p))$ in Legendre space represents a tangent line to the function $f(x)$ with slope p and interception $-F(p)$ respectively.

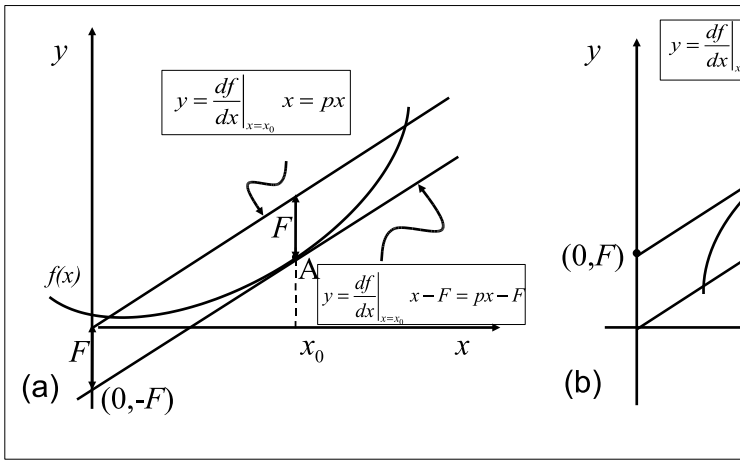

Figure 3.1: The Legendre transform, (a) for a convex and (b) for a concave function.

The Legendre transform can be also applied to a concave function (Fig. 3.1b) where $d^2f/dx^2 < 0$, by defining it as:

$$F(p) = \sup_x [f(x) - px] = -\inf_x [px - f(x)] ,$$

where the interceptions of the tangent lines will be given by $F(p)$.

Thus, we have a Legendre transform that can be applied to any type of functions (either convex or concave type).

The Legendre transform of a convex function $f(x)$ at a point x_0 can be constructed by the following equations:

$$p = \left.\frac{df}{dx}\right|_{x=x_0} \tag{3.1}$$

$$F(p) = px_0 - f(x_0), \tag{3.2}$$

where x_0 is expressed as a function of p using Equation (3.1) and the result is inserted into Equation (3.2), so the resulting expression, $F(p)$, is only a function of p.

Usually, we solve (3.1) as of x and then, (3.2) becomes $F(p) = px(p) - f(x(p))$ which is the transformed function. For a concave function equation (3.2) becomes $F(p) = f(x(p)) - px(p)$.

3.2 Examples

In the next section, some examples of Legendre transformations for some common functions are presented with the corresponding calculations.

Parabola ($f(x) = x^2/2$)

For $f(x) = x^2/2$, we have: $p = \frac{df(x)}{dx} = x \Rightarrow x(p) = p$, so the Legendre transform $F(p)$ is given by:

$$F(p) = px(p) - f(x(p)) = p^2 - p^2/2 = p^2/2,$$
$$\frac{x^2}{2} \overset{\mathcal{L}}{\longleftrightarrow} \frac{p^2}{2}$$

so the parabola remains a parabola in the Legendre space.

Exponential Function ($f(x) = e^x$)

In this case $f(x) = e^x$, so $p = \frac{df(x)}{dx} = e^x \Rightarrow x(p) = \ln p$. The Legendre transform of the exponential function is given by:

$$F(p) = px(p) - f(x(p)) = p \ln p - e^{\ln p} = p(\ln p - 1) = \ln \left(\frac{p}{e}\right)^p,$$

$$e^x \overset{\mathcal{L}}{\longleftrightarrow} \ln \left(\frac{p}{e}\right)^p$$

Logarithmic Function ($f(x) = \ln x$)

This is an example of a concave function. The slope is given by:

$$p = \frac{df(x)}{dx} = \frac{1}{x} \Rightarrow x(p) = \frac{1}{p},$$

which gives the transformed function

$$F(p) = f(x(p)) - px(p) = \ln\frac{1}{p} - p\frac{1}{p} = -1 - \ln p = \ln e + \ln p = -\ln(ep) = \ln\frac{1}{ep},$$

$$\ln x \overset{\mathcal{L}}{\longleftrightarrow} \ln\frac{1}{ep}$$

Hyperbola ($f(x) = -1/x$)

In this case the function consists of a convex ($x < 0$) and a concave ($x > 0$) part. We have :

$$p = \frac{df(x)}{dx} = \frac{1}{x^2} \Rightarrow x(p) = \pm\sqrt{\frac{1}{p}}, (p > 0).$$

For the convex part:

$$F(p) = px(p) - f(x(p)) = -p\sqrt{\frac{1}{p}} - \sqrt{p} = -2\sqrt{p}.$$

For the concave part:

$$F(p) = f(x(p)) - px(p) = -p\sqrt{\frac{1}{p}} - \sqrt{p} = 2\sqrt{p},$$

so the Legendre transform of the hyperbola is denoted by:

$$-\frac{1}{x} \overset{\mathcal{L}}{\longleftrightarrow} -2\sqrt{p}$$

The graphs of the functions and their corresponding tangent line parameters are depicted in Figure 3.2. Due to the geometrical interest (we are going to use the Legendre transform for line reconstruction) we are interested in the line representation of the transformed space (slope, interception) instead of the crude $F(p)$ relation. The reader is reminded that the intercept is $F(p)$ for the concave and $-F(p)$ for the convex part. So in the case of the hyperbola where a convex and a concave part are to be transformed, there are two parts in the slope transform space ($\pm 2\sqrt{(}p)$) instead of the Legendre transform result ($F(p) = -2\sqrt{(}p)$).

3.3 The Circle

The Legendre transformation of the circle is very important for the following chapters so it will be discussed in detail. The circle can be defined by a combination

of a convex and a concave function as shown in Fig. 3.3a. The equation of a circle with center (x_0, y_0) and radius R is given by:

$$f(x) = \begin{cases} f_1(x) = y_0 + \sqrt{R^2 - (x - x_0)^2}, \\ \\ f_2(x) = y_0 - \sqrt{R^2 - (x - x_0)^2}, \end{cases}$$

where equation $f_1(x)$ is referring to the concave part and $f_2(x)$ to the convex part. In the concave case the Legendre transform will be:

$$F_1(p) = \sup_x \left[f_1(x) - px \right], \qquad p = \frac{df_1}{dx}.$$

The derivative $p = df_1/dx$ will be:

$$p = -\frac{x - x_0}{\sqrt{p^2 - (x - x_0)^2}} \Rightarrow x = x_0 \frac{|p|R}{\sqrt{p^2 + 1}}.$$

For the concave case, the sign $(-)$ is correct because for $x > x_0$, $p < 0$ and for $x < x_0$, $p > 0$ (Fig. 3.3a), so $x = x_0 - pR\sqrt{p^2 + 1}$ is used for the Legendre transform which is:

$$F_1(p) = f_1(x) - px = y_0 - x_0 p + R\sqrt{p^2 + 1},$$

so the circle becomes a hyperbola.

As mentioned above, each pair $(p, F(p))$ defines a tangent line to the circle. For a better description it would be more appropriate to express the line equation by its canonical form $r = x\cos\theta + y\sin\theta$ (Fig. 3.3b), so $p = -\cot\theta$ and $F(p) = r/\sin\theta$. In this case, the Legendre transform becomes:

$$\frac{r}{\sin\theta} = y_0 + x_0 \frac{\cos\theta}{\sin\theta} + \frac{R}{\sin\theta}$$

$$\Rightarrow r = x_0 \cos\theta + y_0 \sin\theta + R = r_0 \cos(\theta - \phi) + R, \tag{3.3}$$

where $r_0 = (x_0^2 + y_0^2)^{1/2}$, and $\phi = \arctan(y_0/x_0)$. This equation represents a sinogram in the r, θ Legendre transformation space as shown in Fig. 3.3c. Following the same steps for the convex case, it can be shown that the Legendre transform, in this case it will be:

$$F_2(p) = x_0 p - y_0 + R\sqrt{p^2 + 1},$$

and in the (r, θ) representation:

$$r = x_0 \cos\theta + y_0 \sin\theta - R = r_0 \cos(\theta - \phi) - R. \tag{3.4}$$

Therefore, using equation (3.3) and (3.4) the Legendre transform of the circle is reduced to:

$$f(x) \overset{\mathcal{L}}{\longleftrightarrow} \begin{cases} r = x_0 \cos\theta + y_0 \sin\theta + R, & \text{for concave,} \\ r = x_0 \cos\theta + y_0 \sin\theta - R, & \text{for convex.} \end{cases} \tag{3.5}$$

It is worthwhile mentioning that when the circle reduces to a point, in the limit of $R \to 0$, the Legendre transform is reduced to the Radon/Hough transform (as described in Appendix A) of the point (x_0, y_0), providing us with a single sinogram in the (r, θ) space. Hough transform is a well known technique in pattern recognition which is used very much in image recognition , PET Tomography and other applications. In this case, the Legendre transform represents all the possible lines going through the point (x_0, y_0).

3.4 Properties

The Legendre transform is a non-linear transform. In this section, some basic properties will be described.

Scaling $(af(x) \overset{\mathcal{L}}{\longleftrightarrow} aF(p/a))$

Assuming that $f(x) \overset{\mathcal{L}}{\longleftrightarrow} F(p)$ we calculate the Legendre Transform of $g(x) = af(x)$:

$$G(p) = px - g(x) = px - af(x) = a\left(\frac{p}{a}x - g(x)\right) = aF\left(\frac{p}{a}\right)$$

Stretching $(f(\alpha x) \overset{\mathcal{L}}{\longleftrightarrow} F(p/\alpha))$

Let $g(x) = f(\alpha x)$,

$$G(p) = px - g(x) = px - f(\alpha x) = \frac{p}{\alpha}(\alpha x) - f(\alpha x) = F\left(\frac{p}{\alpha}\right)$$

Translation $(f(x - \alpha) \overset{\mathcal{L}}{\longleftrightarrow} F(p) + p\alpha)$

If $g(x) = f(x - \alpha)$, the Legendre transform will be :

$$G(p) = px - g(x) = px - f(x - \alpha) = p(x - \alpha) + p\alpha - f(x - \alpha) = F(p) + p\alpha$$

Linear Addition $(f(x) + bx + c \overset{\mathcal{L}}{\longleftrightarrow} F(p - b) - c)$

For $g(x) = f(x) + bx + c$, we get:

$$G(p) = px - g(x) = px - f(x) - bx - c = [(p - b)x - f(x)] - c = F(p - b) - c$$

Young's Inequality($px \leq f(x) + g(p)$)

Two functions f and g are called dual in the sense of Young if they are the Legendre transforms of one another. By the definition of the Legendre Transform we have that $g(p) = \sup_x [px - f(x)]$ so always:

$$px - f(x) \leq g(p) \Rightarrow px \leq f(x) + g(p)$$

Involutivity ($\mathcal{L}(\mathcal{L}(f)) = f$)

Let a convex function f. The Legendre transform is: $\mathcal{L}(f) = px - f(x)$. One more transformation will give:

$$\mathcal{L}(\mathcal{L}(f)) = px - [px - f(x)] = px - px + f(x) = f.$$

The above proved properties of the Legendre transform are summarized in Table 3.1.

In this table, the Legendre transforms $f(x) \overset{\mathcal{L}}{\longleftrightarrow} F(p)$ and $g(x) \overset{\mathcal{L}}{\longleftrightarrow} G(p)$ are assumed.

Table 3.1: Properties of the Legendre transform. The $(df/dx)^{-1}$ denotes the inverse derivative of $f(x)$.

Property	Result
Scaling	$af(x) \overset{\mathcal{L}}{\longleftrightarrow} aF(p/a)$
Stretching	$f(ax) \overset{\mathcal{L}}{\longleftrightarrow} F(p/a)$
Translation	$f(x-a) \overset{\mathcal{L}}{\longleftrightarrow} F(p) + a$
Linear addition	$f(x) + ax + b \overset{\mathcal{L}}{\longleftrightarrow} F(p-a) + b$
Young's Inequality	$px \leq f(x) + F(p)$
If $f(0) = df/dx\|_{x=0} = 0$	$F(p) = \int_0^p (df/dx)^{-1}\, dx$
Involutivity	$\mathcal{L}(\mathcal{L}(f)) = f$

3.5 Legendre Transform in higher dimensions

In the previous sections, the Legendre transform was defined for convex and concave type of functions in one dimensions. Here, a generalization of the transform in higher dimensions is presented. Let a real convex function $f(\mathbf{x})$ in a multidimensional space so $f\colon \mathcal{R}^n \to \mathcal{R}$, where $\mathbf{x} = (x_1, x_2, \ldots, x_n)$ and $\nabla^2 f > 0$ (convex function). The

Legendre transform of this function, $F(\mathbf{p})$ is also a multidimensional function given by the relation:

$$F(\mathbf{p}) = \sup_{\mathbf{x}}(\mathbf{p}\cdot\mathbf{x} - f(\mathbf{x})), \quad \mathbf{p} = \nabla f(\mathbf{x}).$$

The geometrical construction is very similar to the one dimension case. We will illustrate the geometrical properties with an example in three dimensions. Let a convex function $f(x,y)\colon \mathcal{R}^2 \to \mathcal{R}, z = f(x,y)$ and a plane $z = \mathbf{p}\cdot(\mathbf{x})$
is described by a point in the origin $(0,0,0)$ and a normal vector $\mathbf{p}$. The Legendre transform is constructed by selecting the point $\mathbf{x}$ on the plane such as the vertical distance (along z axis) from the surface is maximized. For this point, the Legendre transform is given by $F(\mathbf{p}) = \mathbf{p}\cdot\mathbf{x} - f(\mathbf{x})$. This representation gives the tangent plane to the surface $f(x,y)$ in the demanded point. This can be derived easily if we take the equation of a plane tangent to a surface $f(x,y)$:

$$z = \nabla f\cdot(\mathbf{x} - \mathbf{x_0}) + z_0$$

The gradient of the surface ∇f is directed normally to the surface so the $\mathbf{p}$ vector must be equal to the gradient ($\mathbf{p} = \nabla f(\mathbf{x})$ and the z-offset z_0 will be equal to $-F(\mathbf{p})$, very similar to the one-dimensional case. In the same way we can define the Legendre transform for concave function by the relation:

$$F(\mathbf{p}) = \sup_{\mathbf{x}}(f(\mathbf{x}) - \mathbf{p}\cdot\mathbf{x}), \quad \mathbf{p} = \nabla f(\mathbf{x}).$$

where the z-offset will be given by $F(\mathbf{p})$. A simple example for illustration of the method would be to calculate the Legendre transform of a paraboloid $z = f(x,y) = (x^2+y^2)/2$. We have:

$$\mathbf{p} = (p_x, p_y) = \nabla f(x,y) = \left(\frac{\partial f}{\partial x}, \frac{\partial f}{\partial y}\right) = (x,y) \Rightarrow \mathbf{x} = \mathbf{p}.$$

The Legendre transform will be :

$$F(\mathbf{p}) = \mathbf{p}\cdot\mathbf{x} - f(\mathbf{x}) = \mathbf{p}\cdot\mathbf{p} - f(\mathbf{p}) \Rightarrow F(p_x,p_y) = {p_x}^2 + {p_y}^2 - \frac{{p_x}^2+{p_y}^2}{2} = \frac{{p_x}^2+{p_y}^2}{2}$$

so the paraboloid remains a paraboloid in the Legendre space.

The properties of the Legendre transform that were mentioned in the previous section are also valid for the multi-dimensional case. We will add some more properties regarding many dimensions.

Infimal Convolution

The infimal convolution of two convex functions, $f(\mathbf{x})$ and $g(\mathbf{x})$ in n-dimensions ($f\colon \mathcal{R}^n \to \mathcal{R}, g\colon \mathcal{R}^n \to \mathcal{R}$) is defined by:

$$(f \star_{inf} g)(\mathbf{x} = \inf_{\mathbf{y}\in\mathcal{R}^n}\left(f(\mathbf{x}-\mathbf{y}) + g(\mathbf{y})\right).$$

If f and g are concave function we can define the supremum convolution in the same way:

$$(f \star_{sup} g)(\mathbf{x} = \sup_{\mathbf{y} \in \mathcal{R}^n} (f(\mathbf{x} - \mathbf{y}) + g(\mathbf{y})) .$$

It can be proven that the Legendre transform of the infimal convolution is:

$$(f \star_{inf} g)(\mathbf{x} \stackrel{\mathcal{L}}{\longleftrightarrow} F(\mathbf{p}_1) + G(\mathbf{p}_2),$$

where $f(\mathbf{x}) \stackrel{\mathcal{L}}{\longleftrightarrow} F(\mathbf{p}_1), g(\mathbf{x}) \stackrel{\mathcal{L}}{\longleftrightarrow} G(\mathbf{p}_2)$, with $\mathbf{p}_1 = \nabla f(\mathbf{x}), \mathbf{p}_2 = \nabla g(\mathbf{x})$

This result can be generalized for n-convex functions $f_1(\mathbf{x}),\ f_2(\mathbf{x}), \ldots, f_n(\mathbf{x})$:

$$(f_1 \star_{inf} f_2 \star_{inf} \ldots \star_{inf} f_n)(\mathbf{x}) \stackrel{\mathcal{L}}{\longleftrightarrow} \sum F_i(\mathbf{p}_i),$$

where $f_i(\mathbf{x}) \stackrel{\mathcal{L}}{\longleftrightarrow} F_i(\mathbf{p}_i(\mathbf{x})$, with $\mathbf{p}_i = \nabla f_i(\mathbf{x})$

Adjoint Convexity

Let $X \subseteq \mathcal{R}^n$ a real vector space and $X^\star \subseteq \mathcal{R}^n$ the dual space of X, as derived from the Legendre transform. The elements of the two vector spaces will be denoted by $\mathbf{x}$ and $\mathbf{p}$ respectively. The dual pair $< \mathbf{p}, \mathbf{x} >$ is defined as

$$< \mathbf{p}, \mathbf{x} >: X^\star \times X \to \mathcal{R},$$

with $\mathbf{p} \in X^\star$ and $\mathbf{x} \in X$.The dual pair $< \mathbf{p}, \mathbf{x} >$ is actually the inner product of the vectors $\mathbf{x}$ and $\mathbf{p}$. For a function,

$$f(\mathbf{x}) \colon X \to \mathcal{R}, \mathbf{x} \in X,$$

we can define the adjoint convex function $f^\star$ as:

$$f^\star(\mathbf{p}) = \sup_{\mathbf{x}}[< \mathbf{p}, \mathbf{x} > -f(\mathbf{x})] = -\inf_{\mathbf{x}}[f(\mathbf{x}) - < \mathbf{p}, \mathbf{x} > .$$

For this generalized transform the Young's inequality can be generalized to Young-Fenchel inequality:

$$< \mathbf{p}, \mathbf{x} > \leq f(\mathbf{x}) + f^\star(\mathbf{p}).$$

3.6 Legendre transform of order k

In a n dimensional space, the Legendre transform of order k (where $k < n$) can be defined by the function:

$$F^{(k)}(p_1, p_2, \ldots, p_k, x_{k+1}, x_{k+2}, \ldots, x_n) = f(x_1, x_2, \ldots, x_n) - \sum_{i=1}^{k} x_i p_i, \quad p_i = \frac{\partial f}{\partial x_i}. \quad (3.6)$$

The differential of the Legendre transform will then be:

$$dF^{(k)} = df - \sum_{i=1}^{k} d(x_i p_i) \Rightarrow dF^{(k)} = df - \sum_{i=1}^{k} p_i dx_i - \sum_{i=1}^{k} x_i dp_i,$$

where,

$$df = \sum_{i=1}^{n} \frac{\partial f}{\partial x_i} dx_i = \sum_{i=1}^{n} p_i dx_i \Rightarrow dF^{(k)} = \sum_{i=1}^{n} p_i dx_i - \sum_{i=1}^{k} p_i dx_i - \sum_{i=1}^{k} x_i dp_i$$

$$= \underbrace{\sum_{i=1}^{k} p_i dx_i + \sum_{i=k+1}^{n} p_i dx_i}_{\sum_{i=1}^{k} p_i dx_i} - \sum_{i=1}^{k} p_i dx_i - \sum_{i=1}^{k} x_i dp_i$$

$$\Rightarrow dh^{(k)} = \sum_{i=k+1}^{n} p_i dx_i - \sum_{i=1}^{k} x_i dp_i$$

$$\Rightarrow dF^{(k)} = -\sum_{i=1}^{k} x_i dp_i + \sum_{i=k+1}^{n} p_i dx_i. \tag{3.7}$$

From relation (3.7), it can be derived that for the transformed variables ($i \leq k$), the derivative of the order k Legendre transform with reference to the variable p_i is:

$$\frac{\partial F^{(k)}}{\partial p_i} = -x_i,$$

and for the non-transformed variables x_i,

$$\frac{\partial F^{(k)}}{\partial x_i} = p_i.$$

3.6.1 Thermodynamic Potentials

The Legendre transform is applied in thermodynamics for deriving the thermodynamic potential. The first law of Thermodynamics, that expresses the conservation of energy, relates the variation of the internal energy of a system dU, with the respective variation of Heat, dQ, and work, dW:

$$dU = dQ - dW.$$

For a gas that is under a reverse process, the first law of thermodynamics can be expressed as:

$$dU = TdS - PdV, \tag{3.8}$$

where $U = U(S, V)$ is a function of the entropy, S, and volume , V, and the temperature , T, and pressure, P, will be:

$$T = \left(\frac{\partial U}{\partial S}\right)_V, \quad P = -\left(\frac{\partial U}{\partial V}\right)_S.$$

If the function $f(x_1, x_2)$ is considered as the internal energy U, so that

$$f(x_1, x_2) = U(S, V),\ x_1 = S,\ x_2 = V,\ p_1 = \left(\frac{\partial U}{\partial S}\right)_V = T,\ p_2 = \left(\frac{\partial U}{\partial V}\right)_S = -P,$$

the first order Legendre transform will generate the function

$$U - TS \equiv F,$$

and the differential of F is given by (3.7)

$$dF^{(1)} = -x_1 dp_1 + p_2 dx_2 = -SdT + (-P)dV$$

$$\Rightarrow dF = -SdT - PdV,$$

where F is the Helmholtz free energy. The second order Legendre transform will give

$$F^{(2)} = f(x_1, x_2) - \sum_{i=1}^{2} x_i p_i = f(x_1, x_2) - x_1 p_1 - x_2 p_2$$

$$\Rightarrow F^{(2)} = U - TS - (-P)V = U - TS + PV \equiv G.$$

The G function is the Gibbs free energy. The differential of G is given by (3.7) as:

$$dF^{(2)} \equiv dG = -\sum_{i=1}^{2} x_i dp_i = -x_i dp_1 - x_2 dp_2$$

$$\Rightarrow dG = -SdT + VdP.$$

In this example, the second order Legendre transform of $U(S, V)$ was computed to be the Gibbs free energy, $G(T, P)$.
Another example would be to start from $G(T, P)$, and consider it as the initial function $f(x_1, x_2) \equiv G(T, P)$:

$$x_1 = T,\ x_2 = P,\ p_1 = \left(\frac{\partial G}{\partial T}\right)_P = -S,\ p_2 = \left(\frac{\partial G}{\partial P}\right)_T = V.$$

In this case, the first-order Legendre transform will be:

$$F^{(1)} = f - x_1 p_1 = G - (-S)T = U - TS + PV + TS = U + PV \equiv H,$$

where $U + PV \equiv H$ is the enthalpy of the gas. The differential of H is according to (3.7):

$$dF^{(1)} = -x_1 dp_1 + p_2 dx_2 = -(-dS)T - VdP$$

$$\Rightarrow dH = TdS + VdP.$$

The second order Legendre transform is again calculated as:

$$F^{(2)} = f - x_1 p_1 - x_2 p_2 = G - (-S)T - VP = U - TS + PV + TS - PV = U,$$

and its differential is:

$$dF^{(2)} \equiv dU = -x_1 dp_1 + x_2 dp_2 = -(-dS)T - PdV$$

$$\Rightarrow dU = TdS - PdV.$$

The first and second laws of Thermodynamics where proved via the Legendre transform.

3.6.2 Lagrange and Hamilton equations

In analytical mechanics, the derivation of the Hamiltonian $\mathcal{H}(q_i, p_i, t)$, from the Langragian , $\mathcal{L}(q_i, \dot{q}_i, t)$, can be expressed by a $2 - n$ order Legendre transform for n degrees of freedom:

$$\mathcal{L}(q_1, \dot{q}_1, t) \xrightarrow{L} h(q_i, p_i, t),$$

where:

$$F^{(2n)}(q_i, p_i, t) = \mathcal{L}(q_i, \dot{q}_i, t) - \sum_i \dot{q}_i p_i \equiv -\mathcal{H}(q_i, p_i, t), \quad \text{or} \quad \mathcal{H}(q_i, p_i, t) = \sum_i \dot{q}_i p_i - \mathcal{L}(q_i, \dot{q}_i, t),$$

which means that the transformation leads directly to Hamilton equations:

$$\frac{\partial H}{\partial p_i} = \dot{q}_i, \quad \frac{\partial H}{\partial q_i} = -\frac{\partial \mathcal{L}}{\partial q_i} = -\dot{p}_i.$$

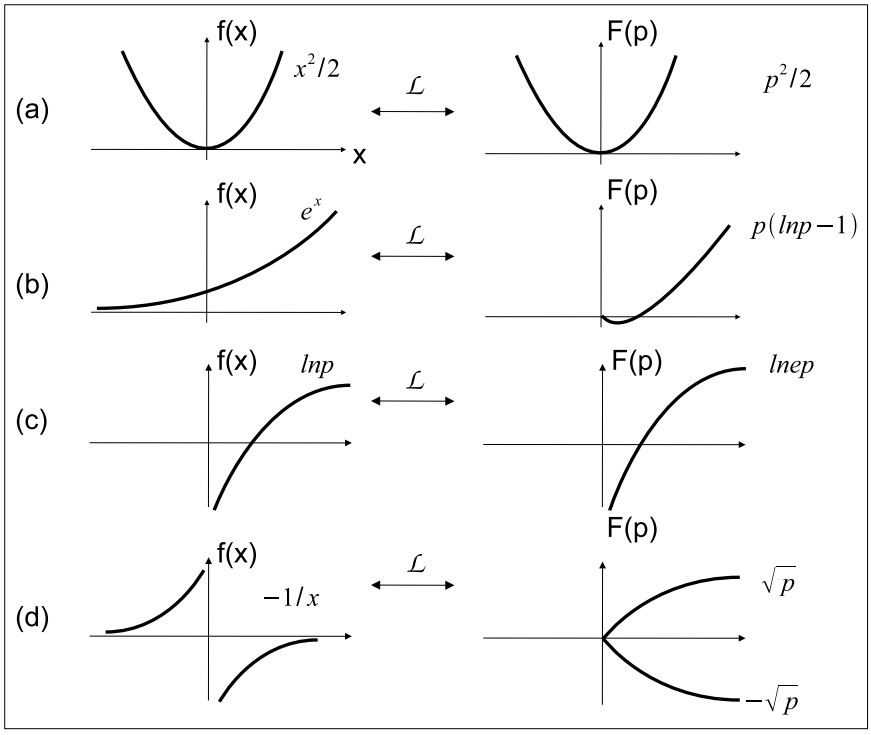

Figure 3.2: Some simple functions and their tangential representation that is derived by the Legendre transform

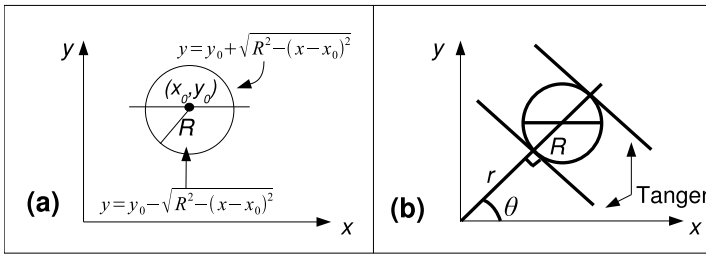

Figure 3.3: (a) Representation of the circle by a convex and a concave function, (b) Tangent Lines in the canonical form equation, (c) Representation of the circle in Legendre transformation space. The circle corresponds to two sinograms in the Legendre transformation space.

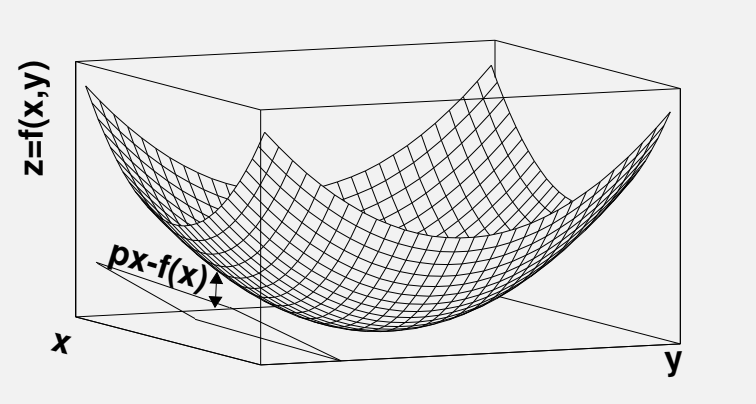

Figure 3.4: Legendre Transform in two dimensions

Chapter 4

Pattern Recognition in Drift Tube Chambers

This chapter describes a new track reconstruction method applied in drift tube chambers using the Legendre transform. The method is designed to provide optimum efficiency in muon reconstruction for a broad band of energy cases. Another goal is robustness again noise produced by high cavern background. The method is tuned and applied to the monitored drift tube chambers of the ATLAS experiment.

4.1 The MDT chamber reconstruction problem

As described in Chapter 2, the drift tube chamber electronics provide information about the drift time of the electrons that are ionized by a passing particle. After calibration, a so called $r-t$ relation provides the relation between the drift time and drift distance. The drift distance is the vertical distance of the particle track, with reference to the center of the MDT tube. The information about the position of the particle for each tube is therefore defined by a circle concentric with the tube and radius equal to the drift distance. Taking in account the errors of the electronics, the calibration relation and the inefficiencies in the wire positions during the construction of the MDT chambers, there is an error propagated to the drift radius for each circle. The MDT chambers in ATLAS, are placed inside a magnetic field so the tracks are curved by the bending power of the toroid magnet. However, in the chamber local coordinate system, the tracks (for transverse momentum values of $p_t > 2$ GeV) can be approached as straight lines. The problem is therefore centralized on finding the best common tangent between the drift circles.

4.2 The Legendre transform approach

According to Chapter 3, the Legendre transform space of a convex function $f(x)$ represents all the tangent lines of the function f. This approach was also generalized for concave functions. In the MDT segment reconstruction case, we seek the common tangent of a set of circles. By transforming each circle in the Legendre space, we get all its tangent lines. The intersection points of the curves in the Legendre space represent the common tangent lines to the circles. Therefore, finding these points leads to the extraction of the reconstruction lines. A circle of center (x_0, y_0) and radius R is transformed in the Legendre space according to equation (3.5) to :

$$r = x_0 \cos\theta + y_0 \sin\theta \pm R,$$

which represents two sinograms in the Legendre space (r and θ are the parameters of the line in the canonical form equation (Fig. 3.3b)). A set of circles will therefore transform to a set of sinograms, where the inverse Legendre transform of the common point will give the demanded line (Fig. 4.1).

4.2.1 The Histogram method

The most efficient way to provide a software implementation of the Legendre space is the representation of the transformed space with a histogram. This method is most used in Image Processing where other histogram algorithms like the Hough transform (Appendix A) are very common. This method denotes that each sinogram will be represented by a set of bins in a two-dimensional histogram. For each circle (sinogram) to be added, new bins are added and peaks start to form. The search for maxima in the histogram extracts the candidate lines. The quantization of space which is introduced by the histogram binning results the forming of clusters around the maxima. The bin size selection is very important about the clusterization. One basic criterion about the selection of the bin size is **proportionality**. The Legendre space histogram is tuned so that the gain of each bin represents the number of circles that contribute a tangent line. This piece of information can be used in later steps of the line extraction and it will be discussed in next sections. Each circle is transformed by computing the value of r parameter for a given θ. The θ parameter is scanned along the histogram limits and one value is evaluated for each bin. The histogram limits can be selected to allow a specific set of lines. This operation prevents the algorithm to reconstruct unwanted horizontal lines and can provide optimization by allowing lines, coming only from an area around a known interaction point.

4.2.2 Selecting the bin size

Considering the error of the drift radius, R and the θ step while transforming in the Legendre space, the error of the r parameter is given by:

$$\delta r = \sqrt{\left(\frac{dr}{dR}\delta R\right)^2 + \left(\frac{dr}{d\theta}\delta\theta\right)^2} \Rightarrow \delta r = \sqrt{\delta R^2 + (x_0 \sin\theta - y_0 \cos\theta)^2 \delta\theta^2} \qquad (4.1)$$

In equation (4.1), the dependence of the error of the r parameter by the position (x_0, y_0) and angle θ is revealed. For a homogeneous behavior in the chamber, this dependence must be minimized. This demand can be applied, if a small θ step is selected. This is very important for a high efficiency in deriving the correct line between the circles (Fig. 4.2.a). In this application, a θ step of 2×10^{-4} radians was selected. For small $\delta\theta$, equation (4.1) becomes $\delta r \approx \delta R$ so the bin size depends only on the error of the drift radius. This error obeys to a complicated distribution because of the non-linearity of the $r - t$ relation, and is depicted in Fig.4.2.b . From the distribution of the error, it can be derived that for most of the error values $\delta R < 0.2$. This means that, if the size is selected to be $\delta r = 0.2$, the bin (in most cases) will contain the info of the circle with radius R but also of the circles with radii $R+\delta R$, $R-\delta R$. If one of the above circles is not included because the error is larger, additional bins are added to include the error information. With this technique, a line maximum is formed in the Legendre space even if the original circles (without including the errors) do not have a common tangent. In other words the sinogram line in Legendre space has a width according to the drift error of the circle under transformation. According to the above, one could select a larger bin size to include all the error information. But this is not encouraged, because tangent lines are formed also for circles that do not correspond to a track, and this results to an increase in the fake rate of the algorithm (fraction of reconstructed segments that do not correspond to a track). Figure 4.3 depicts an event on eight tube layers (a) and the corresponding Legendre transform histogram(b). Histogram 4.3.c shows the legendre space zoomed around the maximum. It is understood that the quantization of space results on a cluster of maxima on the Legendre space. This effect creates the need of a clustering algorithm to extract the lines from the Legendre space. This is described in the next section. Finally Histogram 4.3.d shows the Legendre histogram in polar coordinates.

4.2.3 Clustering in the Legendre space

The properties and behavior of the Legendre transform implemented with the Histogram method was discussed in previous sections. So in this stage it is presumed that a histogram exists which hosts the Legendre space. In this Histogram there are some clusters that correspond to some demanded lines (there might be more than one). These clusters consist of the bins with the best-estimated lines and some neighboring bins that correspond to some lines that are matched to a subset of the

drift circles that contribute to the track. This description leads to the need of a smart-clustering algorithm and its specifications:

- A threshold must be applied to throw lines that consist of a very small number of hits.
- For each cluster, only the bins that have a gain equal to the maximum of the cluster are reconstructed.
- Ambiguous lines must both be reconstructed.
- Cluster separation is needed for multi track events.

The first rule introduces a cut on the gain of the histogram. Because of the proportionality applied during the transformation (section 4.2.2), this threshold will correspond to the number of circles that contribute to the track. This value can be selected at threshold = 3 because three circles can define one common line. So the first procedure on the clustering is to drop all hits with gain < 3. After this procedure the histogram contains only the clusters towards reconstruction (Fig. 4.4.a) The second rule describes the cluster structure. Bins inside the cluster with a lower gain than the maximum bin must be dropped because they will correspond to one neighboring line that has less drift circles that the maximum (Fig 4.4.b). If a neighboring bin has the same gain with the maximum bin there are two cases:

- The bin is a nearest neighbor to the maximum bin so it corresponds to the same line and it is dropped.
- The bin is not a nearest neighbor.

In the second case, there might be an ambiguous case. As depicted in Fig 4.4.c , there is a possibility that a set of drift circles define a couple of "ambiguous" lines. These lines have the same circles but different line parameters (r, θ). Both must be kept for not loosing to the reconstruction efficiency. The last criterion demands that the algorithm must support cluster separation. After processing a number of bins and extracting the lines, the clustering must continue to next maximum and restart association of bins until all the bins with gain over threshold are processed.

The cluster algorithm flow diagram is depicted in Fig 4.5. The clustering algorithm provides a set of reconstructed lines from the Legendre space. It is possible to introduce one post processing step to the whole reconstruction algorithm for further increase in performance.

4.2.4 Drift circle association and least square fit

After clustering, we can correlate the lines to the drift circles that are related to them. For the extraction of the best line equation in the detector coordinate system, it is usual to perform a least-square fit of the line to the nearby circles. A circle is matched to the legendre line if

$$r_i \leq 5\sigma,$$

where σ is the error of the drift distance which is usually known via the calibration (r-t) relation and r_i is the residual between the line and the circle. The best fit to the circles can be extracted by minimizing,

$$\chi^2 = \sum \frac{(d_i - R_i)^2}{\sigma^2}.$$

This cannot be solved analytically, so a Newton Raphson in two dimensions must be utilized to retrieve the line parameters. This procedure is described in [14] and it won't be used until the next chapter where a very accurate estimation of the line is needed. This chapter is concentrated into the patter recognition part of the algorithm, so a draft fit will be introduced.
Instead of fitting the circles, it is possible to fit the line between the points x, y that obey

$$d[(x,y),L] - d[(x,y),(x_0.y_0)] = R,$$

where $d[(x,y),L]$ is the distance between the point (x,y) and the line, and $d[(x,y),(x_0,y_0)]$ is the distance between the point (x,y) and the circle of center (x_0,y_0) and radius R. For the calculation of the points for χ^2, we assume that the line produced by the transform has the form $y = \alpha x + \beta$. Let r_i the radius of the circle (hit) and (x_0,y_0) the center of the tube. The coordinates of the points O, N that belong to the vertical line to the track can be resolved by the equations:

$$x_i = x_0 \frac{r_i}{\sqrt{\alpha^2+1}}, \quad y_i = y_0 \mp \frac{1}{\alpha}\frac{r_i}{\sqrt{\alpha^2+1}}.$$

The point with the minimum distance from the reconstructed line (in this example, the point is represented by O in Fig. 4.6) is selected for the χ^2 test.

4.3 Object Oriented implementation

For a software implementation of the Legendre algorithm a stand-alone Monte-Carlo environment was built. The development language was selected to be C++ because it provides high performance and parts of the algorithm can be integrated to other environments. In the next chapter some classes are used for implementation of the algorithm in the ATLAS software. The main classes of the algorithm are depicted in Fig. 4.7.

4.3.1 Core classes

The main classes of the algorithm are described below.

SegmentFinder

The Segmentfinder class is the heart of the algorithm. It receives the geometry of the chamber and a set of drift tube hits and extracts the Segments. First of all, it calls the Transform class by providing the hits and receiving the peaks in the Legendre space. Then it calls the Clustering class to perform clustering of the peaks and extract the demanded lines. Finally it performs some post processing for fine tuning the segments.

Transform

The Transform class provides the Legendre transform. It creates a 2D histogram with the Histogram class and specifies its dimensions by the chamber dimensions defined by geometry. For each hit it creates the Legendre sinogram and stores it in the Histogram. Then it extracts the hits with gain over the specified threshold.

Clustering

The Clustering class receives the bins over threshold from the Transform class and performs the clustering algorithm. It utilizes the Line class to return the clusterized peaks with the form of line objects.

4.3.2 Secondary classes

In this section all the additional classes that contribute to the package are described.

Line

The line class holds the description of the line both in the canonical form of Fig. 3.3b and of the form $y = ax + b$. It also utilizes some functions to compute distances between line and points and it also contains the Fit method to fit the line to a set of drift circles.

Geometry

The Geometry class provides the reference and control of the chamber geometry.section The Chamber geometry includes information about the tube diameter , the number of tube layers per chamber and the number of tubes per layer. The class contains some methods that provide the coordinates of each tube.

Generator

The generator class creates the Monte-Carlo tracks in the detector. By using the geometry class it resolves the detector acceptance and simulates particle tracks that pass through the chamber. The next step after the creation of a track is the computation of drift radii for the nearby tubes. The Generator class computes the distance between the line and the tube center and associates a circle to each candidate tube. After the hit association, the algorithm creates a Gaussian smearing on the hit radii, as a simulation of the error of the calibration relation. Moreover, noise can be created by random hits in the detector.

Display

The Diplay class provides all the essential tools for drawing the hits and lines. For its implementation, some classes of the ROOT package have been included.

Statistics

The Statistics class provides all the tools for the performance measurements of the algorithm. It provides Histogramming (via ROOT again), Performance studies, Memory measurements and timing.

4.4 Performance study

In the previous section, a novel based reconstruction algorithm based on the Legendre transform was presented. In this section the performance of the algorithm will be tested on a stand-alone controlled Monte - Carlo environment. In order to study the method, a Monte Carlo algorithm is used to produce random lines and create the hits for each tube. As an example, the algorithm is tested in the Monitored Drift Tube chambers of the ATLAS experiment, which is a straw type chamber. In this study, a Drift Chamber of eight tube layers with 20 tubes each, is simulated. The diameter of each tube is selected to be 3 cm. After the hit calculation, a Gaussian measurement error can be applied to each hit. Moreover, random hits can be generated to simulate noise hits in the detector. The study is performed for single and multi-track events using Gaussian measurement error and noise as parameters. For each case, the reconstructed line parameters are calculated. The parameters used for comparison, are the slope $\tan\theta$ and the offset x_0 (the line is parameterized under the equation $y = (x - x_0)\tan\theta$, where the interception of the line is $-x_0\tan\theta$). The residuals (see Fig. 4.6) between the Monte Carlo drift radii and the radii, as reconstructed for each hit after applying the method, are also calculated as a global indicator of the resolution of the tracking algorithm.

4.4.1 Resolution

Single track events are simulated in random angles θ and offset x_0 from a source that is located 1 m away from the detector. The events are reconstructed with the above described method and the reconstructed values are compared to the original values. Fig. 4.8 shows the performance studies for single track events. Histograms (a), (b), and (c) in Fig. 4.8 show the differences between the Monte Carlo and the reconstructed events of the values of the slope $\tan\theta$, the offset x_0, and the residuals. The residual error (resolution) is 7.80 ± 0.07 μm which gives the intrinsic performance of the method. The next three histograms (d), (e), (f) show the same parameters with an applied smearing of 100 μm to each hit. The resolution as shown in Fig. 4.8f is 88.09 ± 0.50 μm, very close to the smearing factor of 100 μm. Histogram 4.8h shows the residual error vs smearing for smearing factors up to 500 μm. As demonstrated by this histogram, the method shows stability providing a resolution that follows the smearing factor. In the next step a random noise is applied into the detector. Noise is simulated as randomly distributed hits with random radii up to the radius of the tube. In the case of multiple hits on a tube, the hit with the smaller radius (earlier signal) is taken into account, as it is supposed to be happening according to the readout electronics of the detector. The graph 4.8i shows the resolution vs noise. Data are simulated with extra noise hits up to 600% and with a smearing factor of 100 μm to each hit. The method seems to be robust in noisy environments and could be very suitable in reconstructing tracks for chambers installed near the beam line of an experiment, where obviously the noise is high. Finally, diagram 4.8g shows a very good correlation between the Monte-Carlo hit radii and the reconstructed ones with a smearing factor of 100 μm.

4.4.2 Reconstruction Efficiency and Fake Rate

The resolution of the algorithm and its robustness was presented in the previous section. In this section, the study is continued with the estimation of the reconstruction efficiency and the fake rate of the algorithm. The reconstruction efficiency is defined as:

$$\text{Efficiency} = \frac{N_{match}}{N_{sim}},$$

where N_{match} is the number of reconstructed segments that were matched to the simulated segments and N_{sim} is the number of simulated segments. The matching criterion between two lines of the form $y = \tan\phi_1(x - x_1)$ and $y = \tan\phi_2(x - x_2)$ is:

$$|\phi_1 - \phi_2| < 0.05 \text{ rad}, \ |x_2 - x_1| < 0.1 \text{ mm}.$$

The fake rate is defined as:

$$\text{Fake Rate} = \frac{N_{fake}}{N_{match}},$$

where N_{fake} is the number of segments that are not matched to a simulated track.

A number of 2000 straight tracks was studied with a smearing of 100 μ m and a noise level ranging from $0 - 1000\%$. Two different threshold values for the minimum number of circles that can be associated to a Line where tested (the standard threshold of 3 and a more strict threshold of 6). The results are presented in Fig. 4.9. The algorithm shows very nice performance on the loose-cut configuration. The fake rate starts to become significant over 500 % noise and the reconstruction efficiency is not affected by noise at all. In the more tight configuration the fake tracks are eliminated. A loss in efficiency is observered over 500 % of noise hits. Therefore, we note that the algorithm shows great resistance to noise in both configuration. In occasions with very high background, a tighter cut can be applied to eliminate the fake tracks. Generally, the threshold can be tuned to provide different pairs of reconstruction efficiency and fake rate. But the fake rate is always proportional to the reconstruction efficiency. It must also be noted that in this study, all possible hits have been included for each event. In the real case, presented in the next chapter there is the possibility to have only three or four hits in eight layers of tubes that have to be associated to a line so in the general case, a low threshold is preferred. However in case of very high cavern background, the noise level becomes very high, which results in the need of specific tuning for efficient tracking.

4.4.3 Computing performance

The Legendre tracking algorithm was proved to be a very efficient algorithm in track reconstruction. In this section, its computing performance will be tested. Histogram algorithms (for example the Hough transform) tend to consume a very large amount of memory to host the histogram. The bins are usually selected to be very small for high resolution and according to the dimensions of the image (hit map) the histogram may become very large. Moreover the time to extract the peaks from the histogram consumes CPU time which in the best case is linearilly proportional to the histogram size. For the tangent line reconstruction problem, the Legendre transform is proven to provide a very good performance in Memory and CPU time which makes it practically applicable to software implementations. The reason is that the Legendre transform holds the minimum info to its histogram needed for the reconstruction. This can be explained by a comparison to the Hough transform is a standard implementation. The Hough transform of a point is a sinogram in the Hough space if the Line is defined in the well-known canonical form (Fig. 3.3b). Each point in the histogram represents a line. So a point is transformed to all the possible lines passing from it. A Hough transform of a circle would be the transform of all its points which corresponds to a large number of sinograms. In the Legendre case, we have only one sinogram per circle which means that in the Drift tube problem case, the Legendre transform is a very small subset of the Hough transform with the relative consequences in computing resources. The method to test the performance

of the legendre algorithm is very simple. For each event, we measure the size of the histogram and the time processed. The histogram is actually represented by a map object of the C++ STL (Standard Template Library). The size of the histogram is:

$$M = \text{number of map entries} \times \text{size of map element}$$

The results of the analysis are presented in Fig.4.10. From histograms 4.10.a, 4.10.c, it can be extracted that the memory consumption and the size of the Legendre algorithm have a normal almost linear behavior as the number of the drift circles to be processed is getting larger. The algorithm performs a reconstruction circle in reasonable linear time so it can be applied for mass offline reconstruction.

4.5 Summary

In this chapter,a new reconstruction algorithm, based on the Legendre transform was studied. The algorithm shows very nice performance in reconstruction efficiency and fake rate and could be a very efficient solution in noisy environments (for example in detectors near the beam line or in high luminosity where cavern background becomes important). The studies on this chapter were done in a stand-alone Monte Carlo environment for testing all the possibilities regarding the algorithm performance. Some reconstruction examples of the algorithm in very noisy conditions are presented in Figure 4.11. In the next chapter we proceed with a more realistic study using GEANT simulated data from muons in the ATLAS Detector.

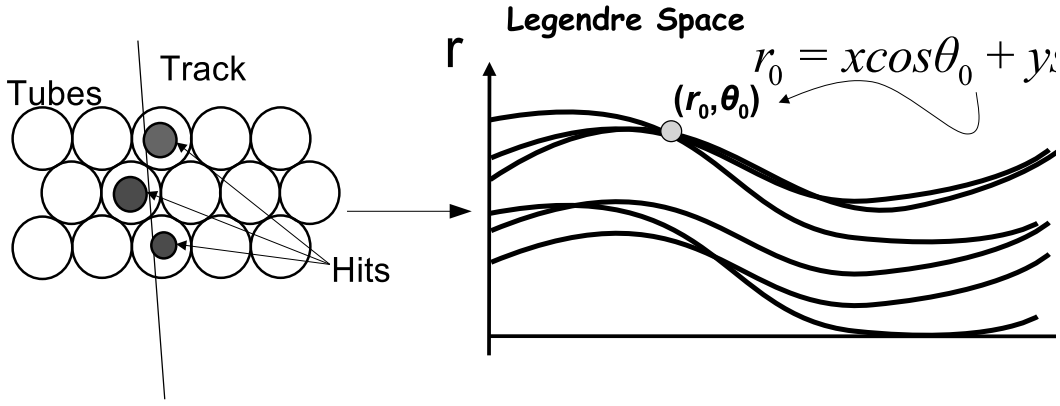

Figure 4.1: Drift circles produced by track and Legendre transform reconstruction principle

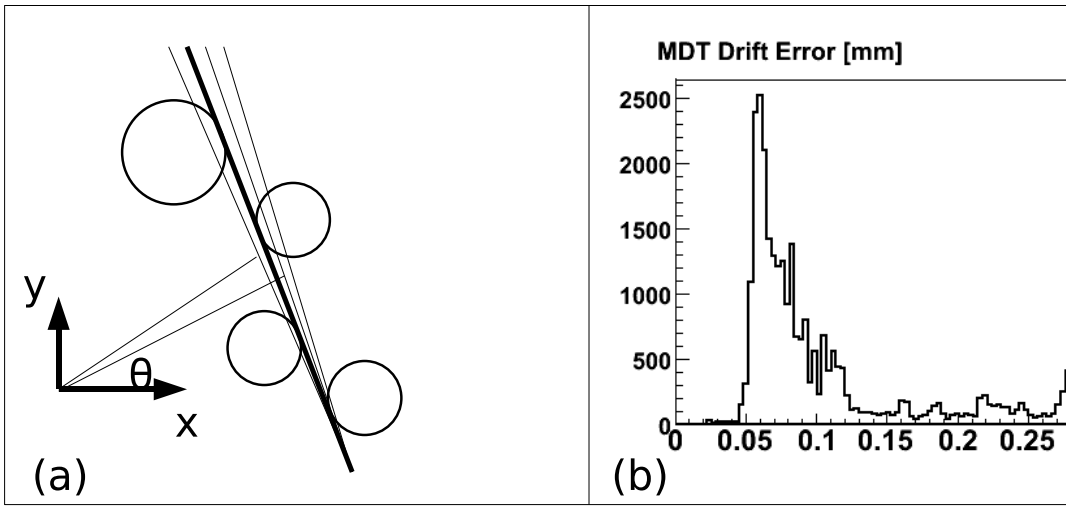

Figure 4.2: (a). θ step while resolving the line (b). Drift error of the MDT Chamber

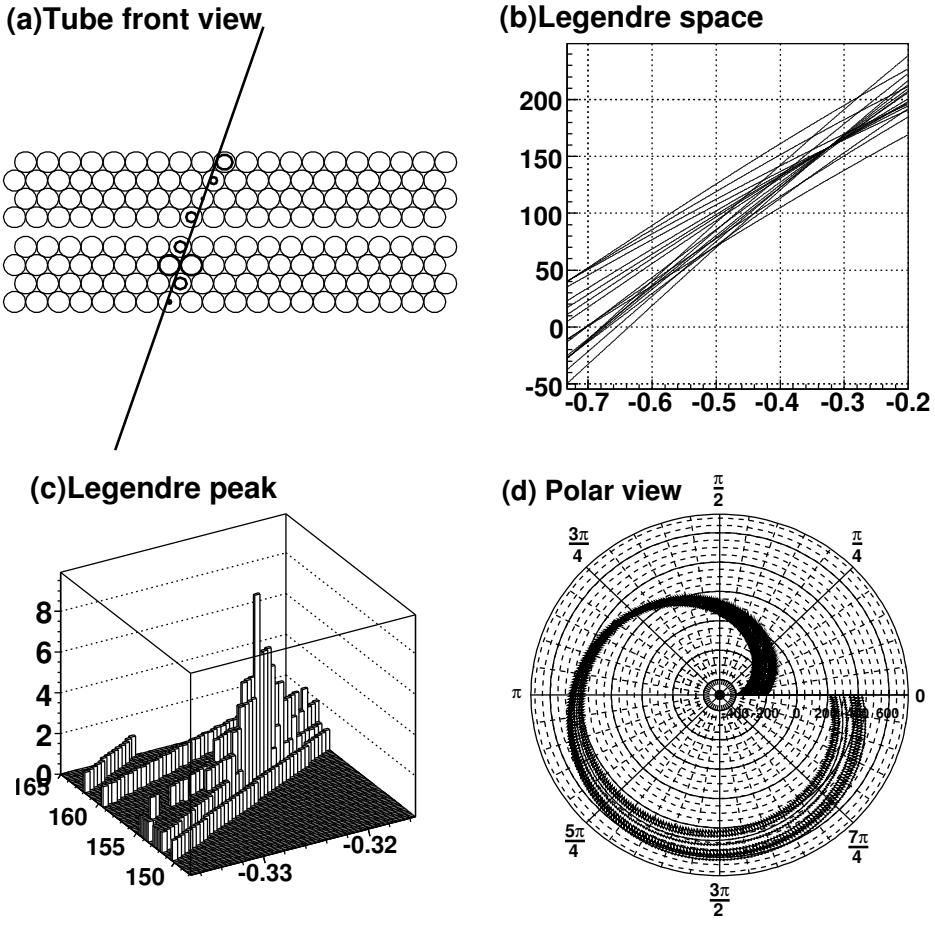

Figure 4.3: (a). Example event (Drift circles on track). (b). Legendre space (c). Legendre space (zoom in maximum) (d). Legendre space (polar coordinates)

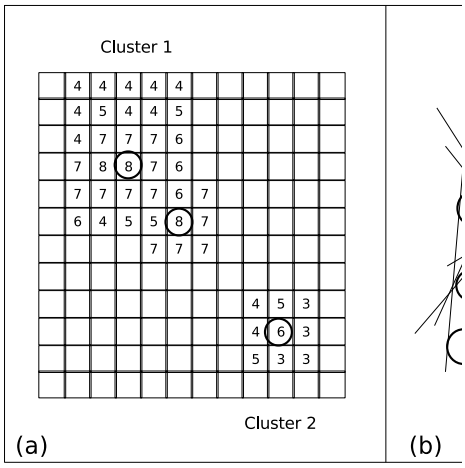

Figure 4.4: (a). Legendre space after thresholding. (b). Lines created by drift tube combinations (c). Ambiguous Lines

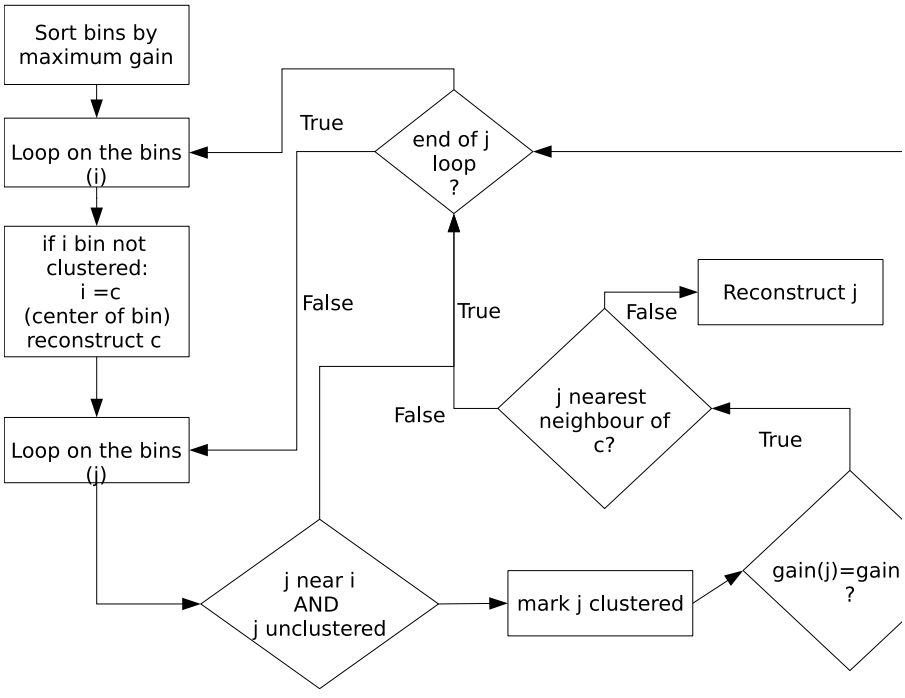

Figure 4.5: Cluster algorithm flow diagram

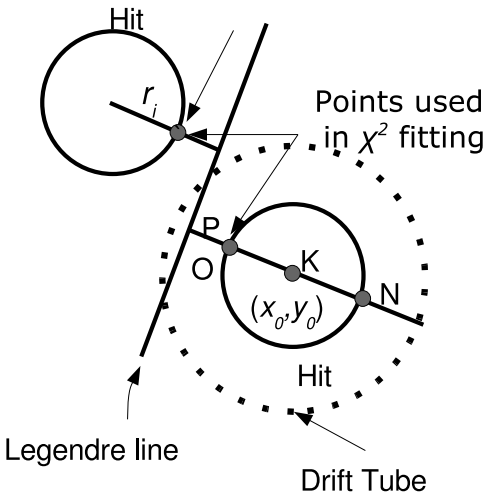

Figure 4.6: Selection of points for the draft χ^2 fit

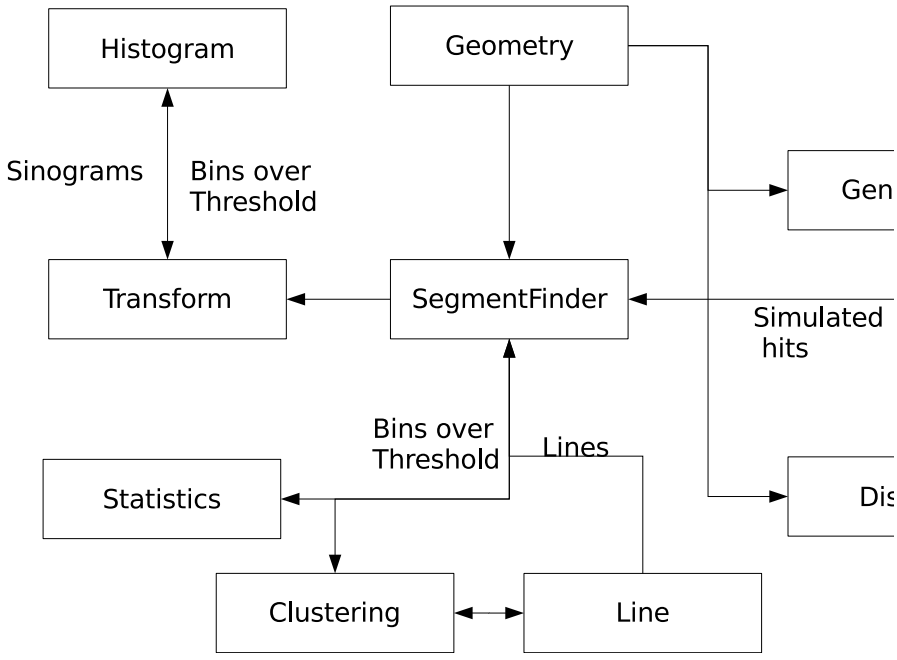

Figure 4.7: Diagram of the main classes of the algorithm and flow control.

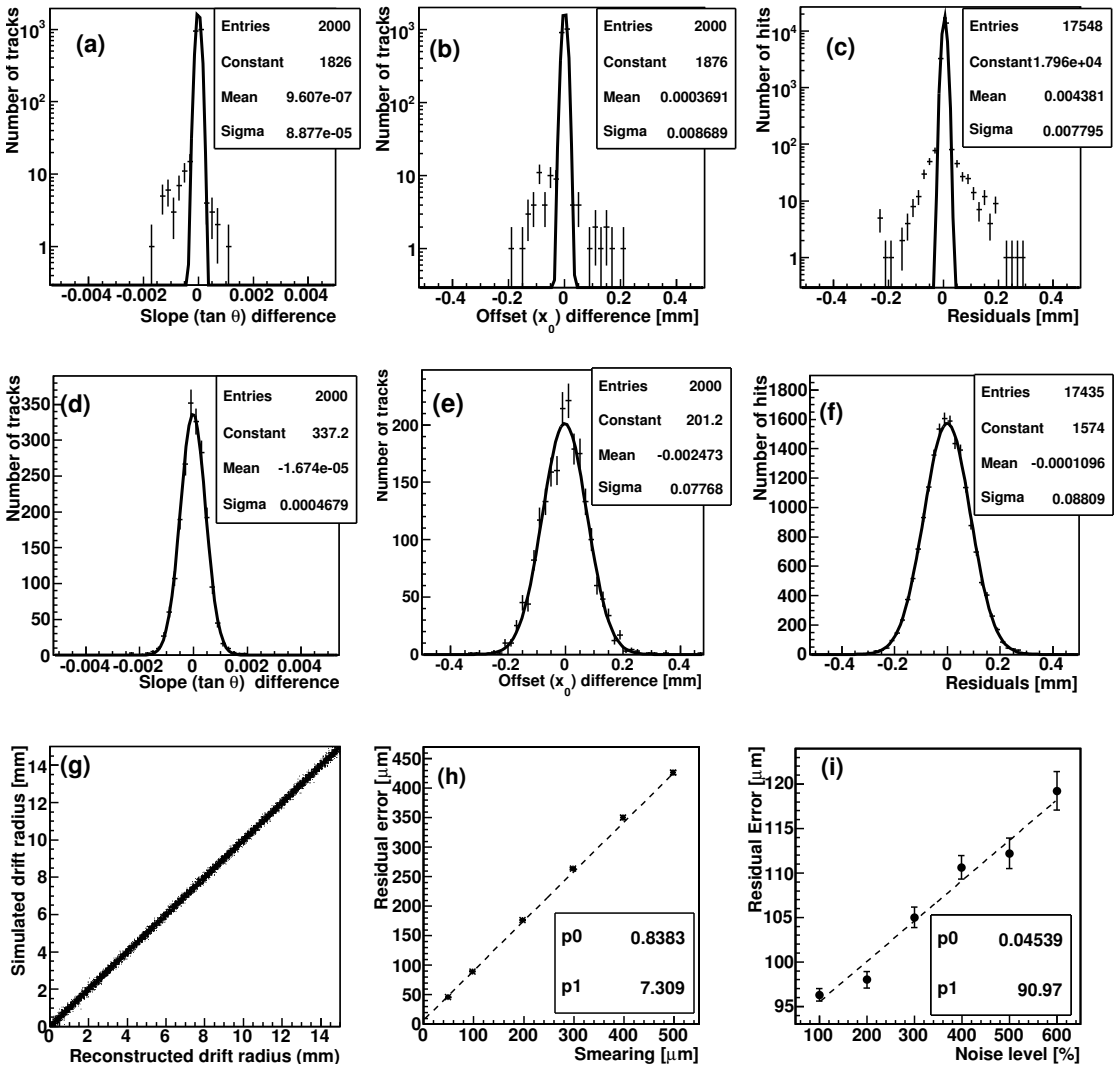

Figure 4.8: Performance results for single track events. Histograms (a), (b), (c) present the differences between the Monte Carlo and the reconstructed events of the values of the slope angle, offset, and the residuals respectively. The residual error (resolution of the track reconstruction) is 3.26 ± 0.03 μm. The next three histograms (d), (e), (f) show the same parameters with an applied smearing of 100 μm to each hit. The standard deviation of the fit in histogram (f) is 88.09 ± 0.50 μm. In graph (g), the correlation between the Monte Carlo generated radii and the reconstructed ones with a smearing of 100 μm is plotted. In graph (h), the residual error in μm versus the smearing in μm, for smearing factors up to 300 μm is plotted. Finally, in graph (i), the resolution versus noise using hits with a smearing factor of 100 μm is plotted. The data are simulated with noise up to 600%.

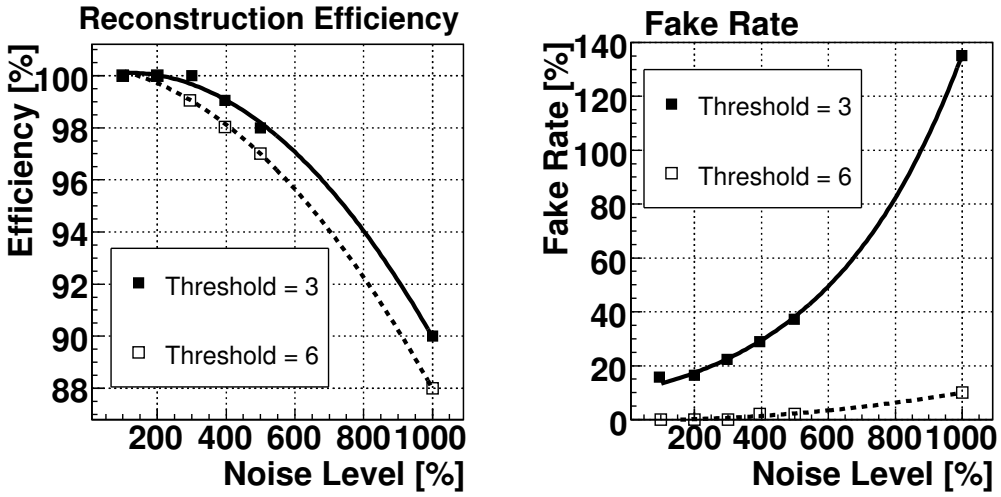

Figure 4.9: Reconstruction efficiency and fake rate as a function of noise level

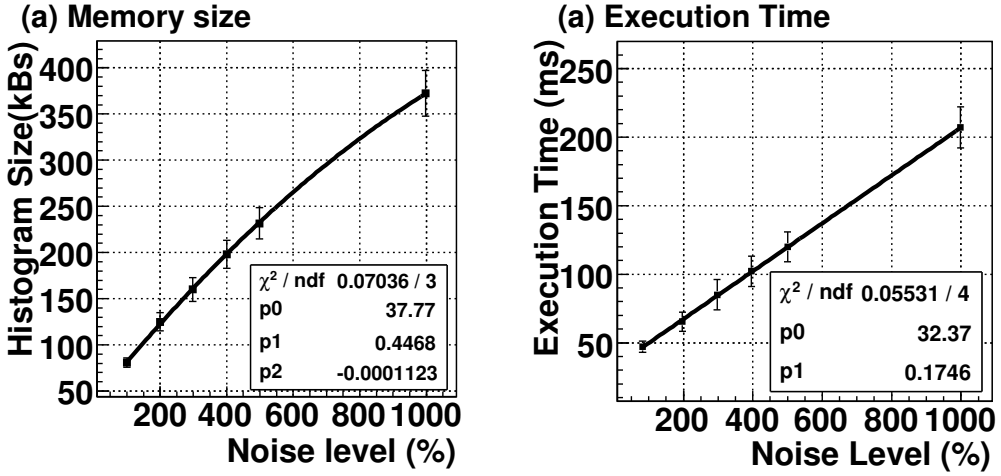

Figure 4.10: (a) Size of the Legendre histogram space in memory, (b) Execution time of the algorithm, as a function of noise level

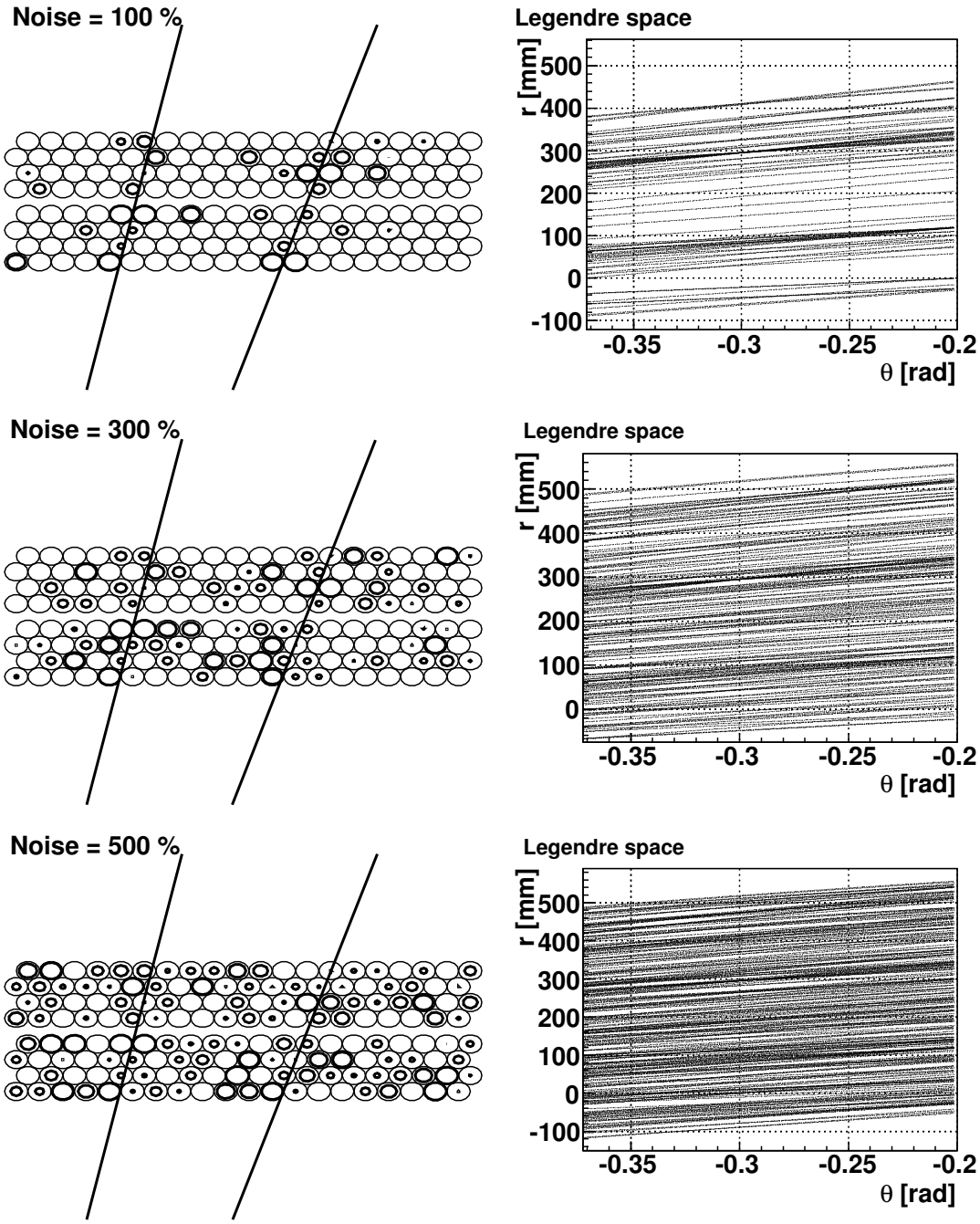

Figure 4.11: Examples of two track separation in noisy conditions and the corresponding Legendre transforms

Chapter 5

A Legendre Segment finder for the ATLAS MDT System

This chapter describes the implementation of the Legendre finding algorithm for a real application - segment reconstruction in the Monitored Drift Tube Chambers of the ATLAS experiment. The main algorithm tools are common with the previous classes but some tools from the ATLAS software(ATHENA) are used for integration of the algorithm to the main ATLAS Reconstruction Framework.

5.1 Description of the Algorithm

The algorithm is hosted in a main algorithm class NTULegendreSegments that is derived from the ATHENA class DCMathSegmentMaker [13]. This class receives a set of Drift Circles and exports the reconstructed segments which are described by the common class MuonSegment. The transformation and clustering interfaces described above have been integrated to the NTULegendreSegments class to provide segments produced by the Legendre transform. For each event the data are processed for each chamber independently. There is only a special case regarding the possibility that a track has shared hits in two neighboring chambers. In this case hits in neighboring chambers are included for the segment finding. The drift circle coordinates are transformed to the local chamber coordinate system where the Legendre transformation is to be applied. The limits of the Legendre histogram allow a range of 1 rad around the angle value of $\pi/2$. In the special case where a road defined by trigger hits exists and passes through the chamber, the limits of the Legendre histogram are tuned around this road. After the transformation, the peaks of the histogram are extracted and imported into the Clustering interface. Finally, after the Clustering, the Segments are created.

Hit association

For the creation of segments the circles are associated to the reconstructed lines. The association criterion is:

$$|\Delta r| = |d_i - r_i| < 5\sigma$$

where d_i is the distance between the line and the tube center and r_i is the radius of the drift circle. if $\Delta r > 5\sigma$ the hit is marked as out of time. If $\Delta r < -5\sigma$ the hit is marked as delta and usually it is created by a δ-electron passing near the wire (closer track than the muon). With this procedure the drift tubes for each line are collected and segments are formed.

χ^2 fit and segment quality cuts

After forming the segments, a χ^2 fit is applied. The fit is done by minimizing

$$\chi^2 = \frac{|d_i - r_i|^2}{\sigma^2},$$

where d_i,r_i and σ are defined in subsection 5.1. The procedure of performing this fit is already developed in the ATLAS muon spectrometer reconstruction software and is described in details in [14]. The main idea is a Newton-Raphson method in two dimensions. After the fit the circles are re-associated to the segments with the above criteria. One more criterion for accepting the segment is the χ^2/N_{dof} of the fit which is demanded to be lower that 10. N_{dof} is the number of the degrees of freedom of the fit which is equal to $N_{dof} = N - 2$ where N is the number of circles to be fitted and the subtraction by 2 refers to the two parameters of the line to be estimated. After processing all the segments, the accepted segments are sorted according to the associated hits and the χ^2/N_{dof} value.

Segment cleaning

The final step before extracting the segments is segment cleaning. A segment cleaning procedure already exists in the ATLAS software (defined in DCMathSegmentMaker algorithm [13]) so some of this tools are imported to the NTULegendreSegments package described here. The main procedures in segment cleaning process are:

- Dropping of hits that are responsible for high χ^2/N_{dof} and reavaluation of segment.
- Dropping of segments that are subset of other already accepted segments.
- Resolving ambiguities.

Regarding ambiguities, ambiguous segments are segments that are associated to the same hits but differ in the line parameters(section 4.2.3). In the case of ambiguous segments, both are accepted but they are marked as ambiguous for resolving the ambiguities in next steps of the track reconstruction.

Summarizing all the above procedures have been included to result to a new segment finding package for the MDT chambers of the ATLAS Muon spectrometer. This package can be inserted for segment finding in a modular way to any existing reconstruction package that supports modularity (Moore, MoMu). The algorithm receives the drift circles from the Calibration framework, reads the Geometry form the Detector Description database and outputs the segments in a common definition where the segments can be processed for the steps of segment association to roads, track creation and momentum output. Moreover using the ATLAS software python-style customization of jobs the algorithm can be fully tuned via a configuration file regarding the segment quality cuts, the thresholds, and Legendre histogram segmentation.

5.2 Reconstruction performance in the ATLAS simulation framework

For the performance studies of the algorithm, the ATLAS Simulation framework was used. Data samples from a broad Momentum spectrum were studied and the algorithm was compared to the basic reconstruction algorithms of the muon spectrometer. The data samples that were used are listed in table 5.1.

Table 5.1: Muon data samples used in the analysis

Sample	Description	Events
$p_t = 100$ GeV	High p_t single tracks	2000
$p_t = 20$ GeV	High p_t single tracks	2000
$p_t = 2$ GeV	Low p_t single tracks	2000
$p_t = 100$ GeV /pile up	High p_t single tracks with cavern background	1000

In the samples with $p_t > 20$ GeV, the tracks are behaving like straight lines inside the chamber so the maximum reconstruction efficiencies are obtained. In the low p_t cases ($p_t < 10$GeV) the curvature of the track becomes significant, something that makes the straight line approximation difficult. For very energetic muons ($p_t > 100$ GeV), electromagnetic showers are produced from the muon tracks and the reconstruction problem becomes difficult. The secondary particles are detected in the tubes and a lot of fake muon tracks appear. The cavern background case is the case that motivated this work. Cavern background is explained by multiple hits inside the detectors that

are not connected to the presence of the muon. These hits can be created by energetic electrons that can pass one or two chambers and give track information. This effects will be visible once the accelerator starts to operate in high luminosity.

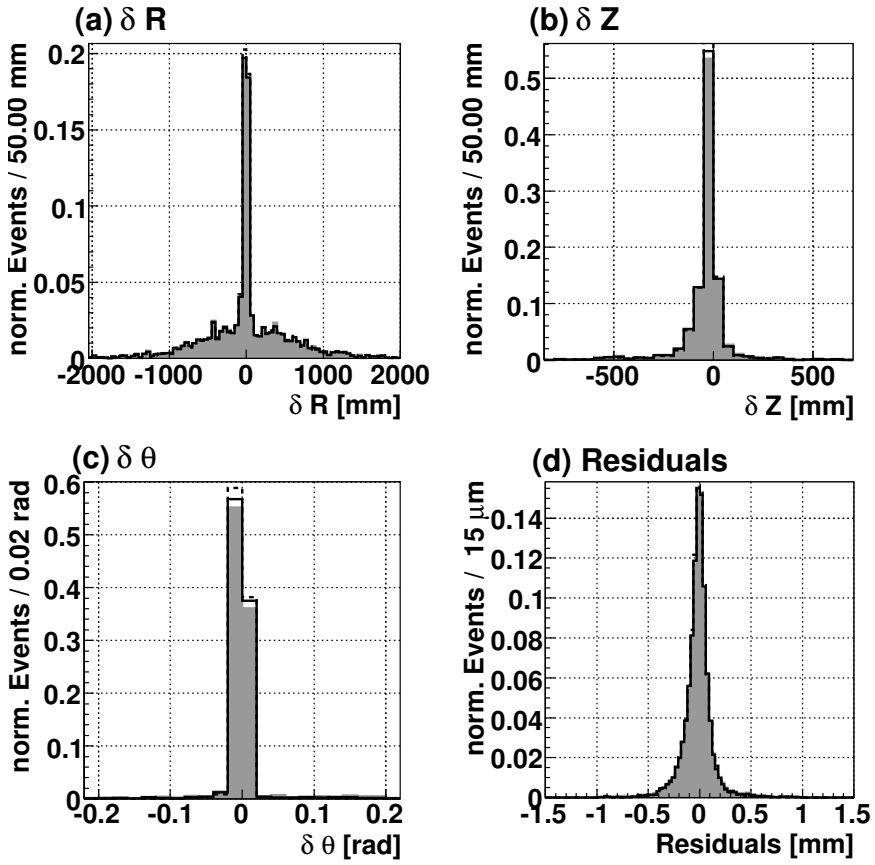

Figure 5.1: (a) Difference in the R coordinate of the segment and the simulated track. (b) Difference in the z coordinate of the segment and the reconstructed track. (c) Difference in the θ angle between the segment and the simulated track (c) Residuals

5.2.1 Performance on a $p_t = 20$GeV sample

The comparison to the existing reconstruction program can be accurately made only with the Moore and MoMu reconstruction packages where the comparison can be made only in the segment-finding level. Muonboy package (which provides very nice results as well) is a stand-alone program including all the reconstruction steps so the comparison with the Legendre algorithm in the MoMu package can be biased by some advantages of the road or track creation algorithms. The MoMu package contains the DCMathSegmentMaker [13] segment finder which uses the same idea

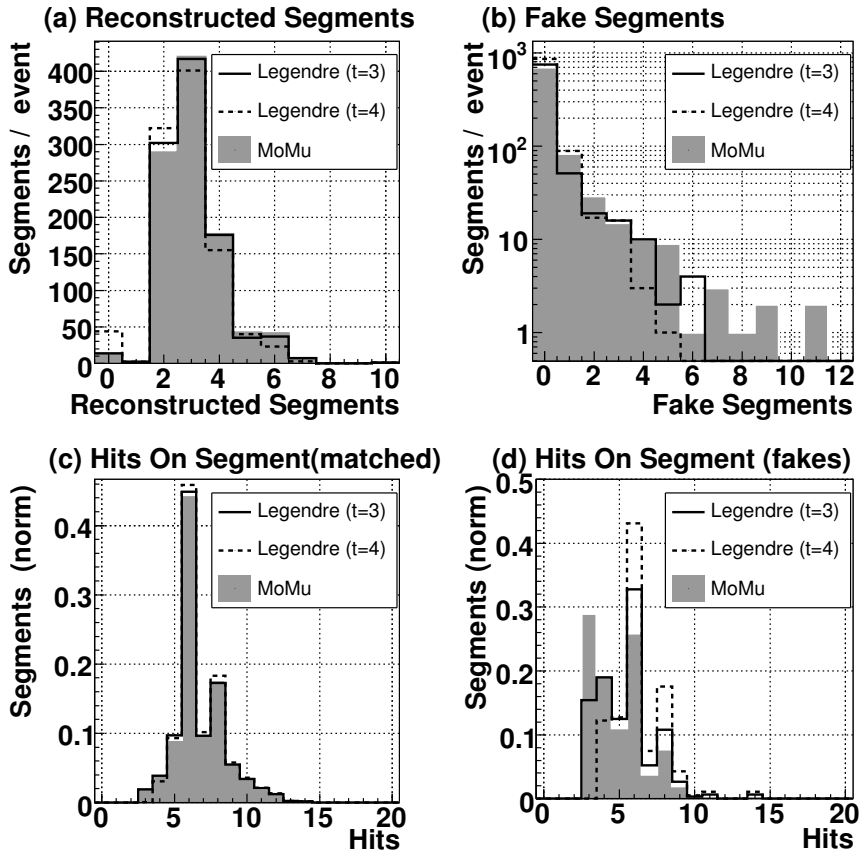

Figure 5.2: (a). Matched reconstructed segments per event (b) Number of fake segments per event (c) Number of hits on segment for matched segments (d) number of hits on segment for fake segments.

with Moore segment finder but in the MoMu case the algorithm supports segment cleaning and refining, something that results to better performance.
The first study is performed on a sample of single track muons of $p_t = 20$GeV muons which is a very important region on the p_t spectrum because the mean value of the transverse momentum of muons produced by $t\bar{t}$ and simulated Higgs decays are near this value. The comparison is done using MoMu reconstruction package with DCMathSegmentMaker and NTULegendreSegments. DCMathSegmentMaker provides the best performance so the Legendre Algorithm will be compared only to it. Muonboy will not be tested segment by segment but some results while running it in standalone mode will be presented at the end of the chapter. The Legendre algorithm will be tested in two possible configurations, one with loose and one with tight cuts. The samples are reconstructed with the above algorithms and the reconstructed segments are matched with the simulated segments to evaluate the match. The segments that

are matched with the truth info are called matched segments. The reconstructed segments that are not matched to the truth information are characterized as fake segments. The segments are extrapolated and the reconstructed vertex parameters compared to the the simulated tracks. The values of these parameters tend to be similar in high-p_t muons that the full tracks tend to be straight lines but differ very much in low-p_t samples where the tracks are curved. For a quantitive description of the performance, the reconstruction efficiency and the purity of the algorithms is presented. The reconstruction efficiency is defined as:

$$\text{Efficiency} = \frac{\bar{N}_{match}}{\bar{N}_{sim}},$$

where $\bar{N}_{match}$ is the average number of segments that are matched per event and $\bar{N}_{sim}$ is the average number of simulated segments per event. On the same manner, the purity is defined by:

$$\text{Purity} = \frac{\bar{N}_{match}}{\bar{N}_{match} + \bar{N}_{fake}},$$

where $\bar{N}_{fake}$ is the average number of fake segments per event. Finally, the Fake rate is defined as:

$$\text{Fake Rate} = \frac{\bar{N}_{fake}}{\bar{N}_{match}},$$

A first estimation of the performance is depicted in Fig. 5.1. Histogram (a) shows the difference between the track R coordinate and the R coordinate derived by extrapolating the segment. The peak is broad because the curvature of the muon. The Muon spectrometer is a large system, something which results in a large error on the global coordinate system even if the magnetic field pulls are very small. All the algorithms have the same behavior because they use the same χ^2 fitter for their segments. The same results are valid for the other parameters as the z coordinate and the θ angle. In the θ angle distribution (Histogram (c)) it is visible that the tight cut Legendre algorithm has more of its reconstructed segments centered which results on a better segment quality. In Histogram (d) the residuals (as defined in Section 4.4) are plotted. All algorithms have the same distribution. The residual error is 86.1 ± 1.0 μm which is equal to the precision of MDT chambers in position measurement.

The reconstruction efficiency of the algorithm is depicted in Fig. 5.2. Histogram (a) shows the number of matched segments per event. MoMu and Legendre in the loose-cut configuration have equal distributions. There is a small loss in the reconstruction efficiency for the tight cut configuration. Histogram (b) shows the number of fake segments per event. Legendre, in both configurations, shows a smaller fake rate than MoMu. Histogram (c), shows the number of hits per segment for the matched segment. This is an indicator of the segment quality. In all algorithms, there are two peaks on size and eight hits. This is connected to how many layers of tubes exist per chamber. In the inner layer, the chambers have eight layers and in the middle

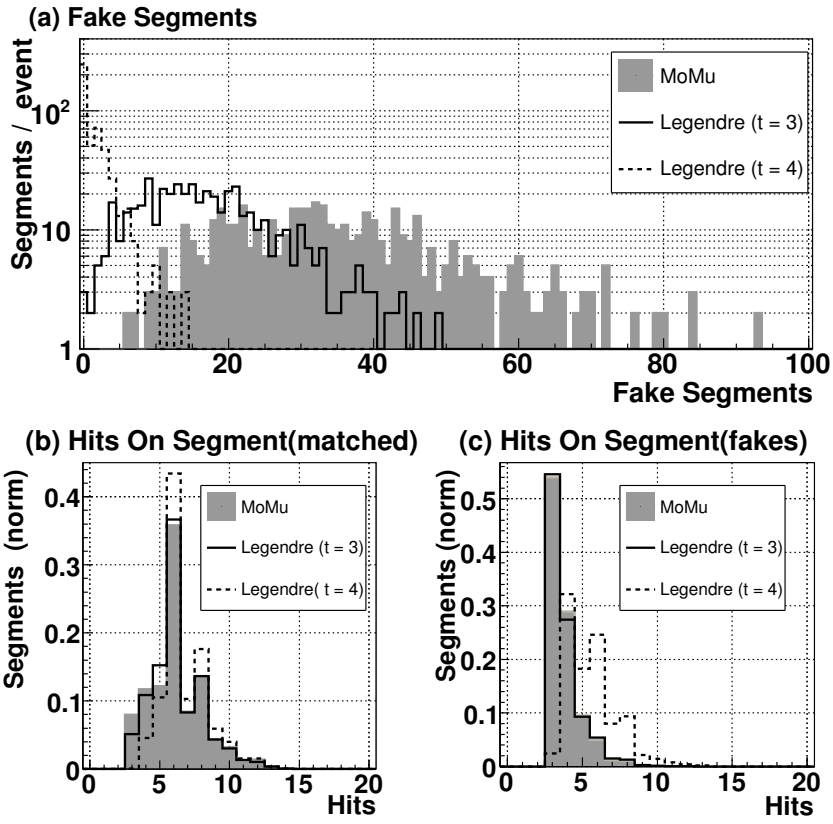

Figure 5.3: Cavern background studies (a) Number of fake segments per event (b) Number of hits on segment for matched segments (e) number of hits on segment for fake segments.

and outer layers there are six layers of tubes. All algorithms have similar performance. It is noted that in the tight-cut case of the Legendre algorithm there are more segments on the two peaks, something that indicates a better segment quality. Finally histogram (d) shows the number of hits per segment for the fake segments. This histogram is important because it provides information about what kind of fake segments are detected for each case. In the Legendre algorithm in both configurations there are significant peaks in 6 and 8 hits, something that indicates that the algorithm is cheated only in the case that a secondary particle passes from the tubes and not by randomly distributed noise hits. Moreover in the tight cut case the peaks become higher, something that amplifies the previous argument. For a quantitive desciption,the purity, efficiency and fake rate of the algorithm have been computed. MoMu provides the higher reconstruction efficiency of 97% while the Legendre in the loose and tight cut configuration provides 96% and 92% respectively. The respective

fake rate is 15% for MoMu and 12% and 7% for Legendre in both configurations. The purity, which is an overall indicator of the performance is 87% for MoMu, 89% for the loose Legendre and 94% for the tight Legendre case.

The Legendre algorithm was proven to provide very nice performance on a clean 20 GeV sample. A tight-cut configuration provides even higher purity but there is no special need to be used in this relative clean sample. The great need for a tight cut configuration arises when cavern background samples need to be processed as described in next section.

5.2.2 Eliminating cavern background

For studying cavern background , a sample of $p_t = 100$ GeV, with cavern background was processed. The signal to background ratio was selected to be 0.2 so there is 500% noise per event. Fig 5.3 describes the performance studies. Histogram (a) depicts the number of fake segments per event. MoMu has the highest fake rate. The average value of fake segments per event is 37. The Legendre algorithm on the loose cut configuration reduces the fake rate by a factor of two but still a lot of fake segments exist.There are 19 fakes per event. From Histogram (d), it is derived that for both algorithms, most of the fake segments have three hits. This is expected because in a high background sample of randomly distributed hits, the possibility of finding a line with three hits becomes very high. So it is essential to apply the tight configuration for the Legendre algorithm, with a threshold of four drift circles per line. This procedure reduces the fake rate near the level of clean samples. The cavern background is almost eliminated providing an average value of 1 segment per event. Histogram (b) shows the distribution of hits on the matched segments. The expected peaks at 6 and 8 are much sharper in the Legendre tight configuration. In Histogram (c), one can observe that in the Legendre tight-cut configuration, the distribution approaches the one of the clean samples except a noise peak at 4 hits(There are some fake segments with four peaks).

5.2.3 Overall performance

The previous section presents a detailed comparison on the segment level between the segment finder of the MoMu reconstruction program and the new Legendre algorithm. These studies were done on a clean sample of $p_t = 20$ GeV and in a cavern background sample of $p_t = 100$ GeV. The cavern background sample was selected to be 100 GeV so that there are no curvatures in the tracks and any inefficiencies would be due to cavern background. In this section, the studies were repeated for momenta ranging between $p_t = 2 - 100$ GeV. Data from Muonboy package are included but it is reminded that the comparison with Muonboy is done on the package level and segment data are extracted afterwards so the comparison could be biased. Table 5.2

shows the segment reconsdtruction efficiency for the different algorithms. and Table 5.3 shows the segment purity.

Table 5.2: Segment reconstruction efficiency for all algorithms

Algorithm/p_t	2 GeV	20 GeV	100 GeV
MoMu	77%	97%	97%
Muonboy	67%	92%	91%
Legendre(t = 3)	76%	96%	95%
Legendre(t = 4)	71%	92%	91%

Table 5.3: Segment reconstruction purity for all algorithms

Algorithm/p_t	2 GeV	20 GeV	100 GeV
MoMu	78%	87%	73%
Muonboy	71%	88%	73%
Legendre(t = 3)	79%	89%	75%
Legendre(t = 4)	81%	94%	79%

It is observed that the Legendre algorithm provides the best segment purity in both configurations. MoMu still provides the highest reconstruction performance. Generally, for high values of the efficiency an incleased fake rate is expected. This is also observable by the tunability of the Legendre algorithm. Making the cuts slightly tighter, the purity increases but there is also a loss in the efficiency. However, it is visible that the Legendre algorithm for the cavern background and in the loose cut configuration can provide a reconstruction efficiency near MoMu but it reduces the fake rate by a factor of two. A tighter cut by one more drift circle per line can further reduce noise by a factor of 10 making the reconstruction problem much easier.

5.2.4 Computing performance

The Legendre algorithm was proved to be a very efficient tool in segment reconstruction in the ATLAS Muon spectrometer. This section refers to the CPU performance of the algorithm. As mentioned in the previous chapter, histogram algorithms tend to consume large amounts of memory for hosting the transform space. However, it was proven that the Legendre transform can be applicable because it holds the minimum information. Fig. 5.4 shows the processing time and the histogram size in memory for a cavern background sample. A fit with the Landau distribution in both cases gives a mean (Mean peak value) processing time of 16ms and an average size in memory of 100kB. It is denoted that the cavern background case is the most consuming in resources because a very large number of circles needs to be transformed.

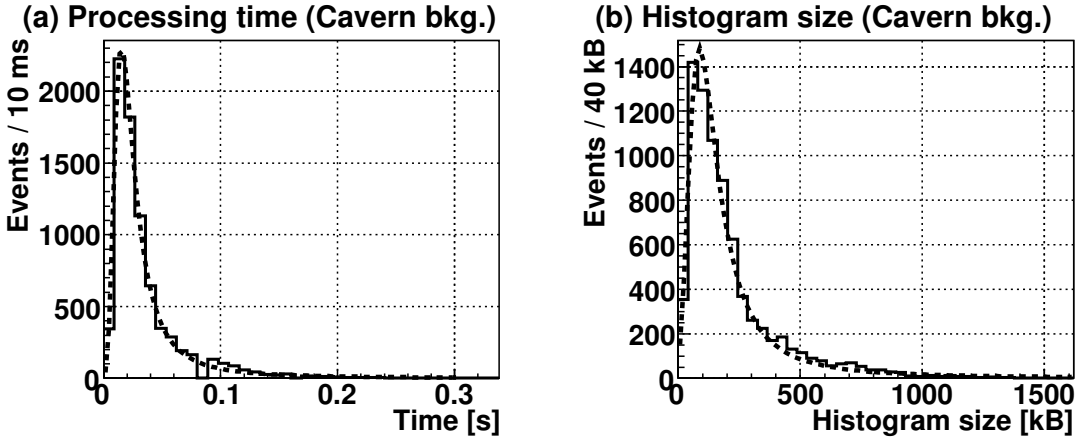

Figure 5.4: Computing performance studies (a) Algorithm processing time (b) Histogram size in memory

The algorithms maintain low values in the CPU performance parameters, something that makes it applicable in high production rates.

5.3 Summary

In this chapter the Legendre algorithm was developed and tested in the ATLAS software. The algorithm shows the highest purity something that makes it a very useful tool for cavern background reconstruction. Moreover the CPU performance is nice and acceptable, something that makes the reconstruction algorithm applicable for mass offline reconstruction. The algorithm can be integrated for segment reconstruction in MoMu and Moore reconstruction packages via simple job option entries.

Appendix A

The Radon/Hough transform

Let a function $f\colon \mathcal{R}^2 \to \mathcal{R}$ defined in a space $\mathcal{D} \subseteq \mathcal{R}^2$ and L a random straight line of $\mathcal{R}^2$ space. The linear Radon transform [1, 12] is defined by the projection of $f(x, y)$ on line L. Therefore, the Radon transform which is denoted by $f(x, y) \xleftrightarrow{\mathcal{R}} \check{f}(r, \theta)$ and is expressed by the following integral:

$$\check{f}(r, \theta) = \mathcal{R}[f(x, y)] = \int_L f(x, y) ds, \tag{A.1}$$

where ds is the fundamental line segment. Usually, the line L will be parameterized using the canonical form equation:

$$r - x \cos\theta - y \sin\theta = 0, \tag{A.2}$$

where r and θ are shown in Fig. 3.3b. Therefore, the integral of $f(x, y)$ on line L depends on the parameters r, θ, (Equation (A.2)).

The Radon transform can be defined on any curve (even in higher dimensions) and a standard procedure is to define the transform on the curve that needs to be recognized. Using the definition of delta function $\delta(r)$, and by combining equations (A.1) and (A.2), the Radon transform of a function $f(x, y)$ will be:

$$\check{f}(r, \theta) = \int \int_{\mathcal{R}^2} f(x, y) \delta(r - x \cos\theta - y \sin\theta)\, dx dy. \tag{A.3}$$

It is known that on a plane, a single point (x_0, y_0) can be described by the function:

$$f(x, y) = \delta(x - x_0)\delta(y - y_0).$$

Therefore, the Radon transform of a single point (x_0, y_0) as implying from Equation (A.3) will be:

$$\check{f}(r, \theta) = \delta(r - x_0 \cos\theta - y_0 \sin\theta). \tag{A.4}$$

Equation (A.4) has the form of (A.2) and represents a sinogram in Radon space (r, θ). This formula can provide a discrete transformation method suitable for computer algorithms known as the Hough transform. According to Hough transform, each point (x_0, y_0) in image space is transformed to a sinogram $r = x_0 \cos\theta + y_0 \sin\theta$ that describes all possible lines that pass from the point (x_0, y_0). Therefore, for two given points in image space, there are two sinograms in transform space and their intersection point represents the parameters r and θ of the line that connects the two points in image space.

Bibliography

[1] T. Alexopoulos, "Introduction to Signal Analysis", NTUA, 2004 (in Greek).

[2] T. Alexopoulos *et al*, NIM A 560, 633 (2006).

[3] V.I. Arnold, "Mathematical Methods of Classical Mechanics", Springer-Verlag, 1989.

[4] ATLAS Collaboration, ATLAS Technical Proposal, CERN/LHCC/94-43, 1994.

[5] ATLAS Inner Detector Community, ATLAS Inner Detector Technical Design report, CERN/LHCC/97-16 & 17, 1997.

[6] ATLAS Collaboration, ATLAS Calorimeter performance TDR, CERN/LHCC/96-40,1996.

[7] ATLAS Muon Collaboration, ATLAS Muon Spectrometer technical design report, CERN/LHCC/97-22, 1997.

[8] F. Sauli, Principles of operation of multiwire propotional and drift chambers, CERN, Geneva, 1977

[9] Volker Pashhoff, Studies on ageing and reanimation of drift tubes for the ATLAS muon spectrometer, PhD thesis, Freiburg, 1999

[10] L. Dorst, R. Van den Boomgaard, Signal Processing 38, 79 (1994).

[11] K. Kleinknecht, Detectors for particle radiation,Cambridge University press, 1998

[12] S.R. Deans, "The Radon Transform and Some of Its Applications", John Willey & Sons, 1983.

[13] N.V. Eldik, "The Atlas Muon Spectrometer: Calibration and Pattern recognition", NIKHEF PhD thesis, 2007.

[14] M.J. Woodstra, "Precision of the ATLAS Muon spectrometer", NIKHEF PhD thesis, 2002.

[15] D. Adams *et al*, Track reconstruction in the ATLAS Muon spectrometer with MOORE, ATL-MUON-96-105, 1996.

[16] M.Virchaux, Muonbox: a full 3D tracking programme for Muon reconstruction in the ATLAS Spectrometer, ATL-MUON-1997-198,1997.